Mon. Not. R. Astron. Soc. **000**, 1–20 () Printed 17 June 2009 (MN LATEX style file v2.2)

Time-dependent 3D spectrum synthesis for type Ia supernovae

M. Kromer⋆ and S. A. Sim
Max-Planck-Institut für Astrophysik, Karl-Schwarzschild-Straße 1, D-85748 Garching b. München, Germany

16. June 2009

ABSTRACT
A Monte Carlo code (ARTIS) for modelling time-dependent three-dimensional spectral synthesis in chemically inhomogeneous models of Type Ia supernova ejecta is presented. Following the propagation of γ-ray photons, emitted by the radioactive decay of the nucleosynthesis products, energy is deposited in the supernova ejecta and the radiative transfer problem is solved self-consistently, enforcing the constraint of energy conservation in the co-moving frame. Assuming a photoionisation dominated plasma, the equations of ionisation equilibrium are solved together with the thermal balance equation adopting an approximate treatment of excitation. Since we implement a fully general treatment of line formation, there are no free parameters to adjust. Thus a direct comparison between synthetic spectra and light curves, calculated from hydrodynamic explosion models, and observations is feasible. The code is applied to the well known W7 explosion model and the results tested against other studies. Finally the effect of asymmetric ejecta on broad band light curves and spectra is illustrated using an elliptical toy model.

Key words: radiative transfer – methods: numerical – supernovae: general.

1 INTRODUCTION

Type Ia supernovae (SNe Ia) are commonly believed to originate from thermonuclear explosions of degenerate material in white dwarf stars (Hoyle & Fowler 1960), thus being important for binary evolution and the chemical evolution of the Universe. By their dynamical interaction with the interstellar medium they may also play an important role in the star formation history of galaxies. However, even after many years of intensive research it is still not completely understood how these explosions take place and which are the progenitor systems [see e.g. Hillebrandt & Niemeyer (2000) for a review on the explosion mechanism and Livio (2000) on progenitors].

In the standard single degenerate Chandrasekhar mass model, a C+O white dwarf accretes mass from a non-degenerate companion star (either a main-sequence or red giant star) until it nears the Chandrasekhar mass. Then the pressure of the degenerate electrons can no longer balance gravity and a thermonuclear runaway, disrupting the white dwarf, can occur. An attractive feature of this picture is that exploding at a well specified mass provides a natural explanation of the observed homogeneity of the SNe Ia class.

However, SNe Ia are not all the same. Observations of nearby SNe Ia show a broad scatter in peak luminosity and decay time-scale. Phillips (1993) derived empirical relations to calibrate the peak luminosity of SNe Ia by distance independent light curve properties which makes them standardiseable candles. Because of their high luminosities (typically $\sim 10^{42}\,\mathrm{erg\,s^{-1}}$) they can thus be used to measure the cosmic expansion history up to high redshifts. Various forms of this approach have been used by different groups (e.g. Riess et al. 1998; Perlmutter et al. 1999). They found that SNe Ia at high redshift appear fainter than expected in a matter dominated Universe, indicating an accelerated expansion. This was confirmed by following studies (e.g. Riess et al. 2004; Astier et al. 2006) and led to the ΛCDM cosmologies in which a positive cosmological constant or "dark energy" with negative pressure is used to model the accelerated expansion of the Universe.

One way to constrain dark energy models is to study the evolution of the dark energy equation-of-state parameter w by measuring the cosmic expansion history, a goal of ongoing [e.g. ESSENCE (Wood-Vasey et al. 2007), SNLS (Astier et al. 2006)] and future projects. For that purpose, the distances to high-redshift SNe Ia must be determined to high accuracy, which requires, amongst other factors (e.g. the extinction to the supernova and K-corrections), a reliable calibration of the peak luminosity. To improve the calibration techniques, which are based on purely empirical relationships, a thorough theoretical understanding of SNe Ia and improved observations are needed.

⋆ E-mail: mkromer@mpa-garching.mpg.de

Much progress (both in numerical methods and computational power) has been made in the hydrodynamical explosion modelling of SNe Ia since the first one-dimensional (1D) calculations by e.g. Nomoto, Thielemann & Yokoi (1984) became available. Today, fully three-dimensional (3D) explosion models (e.g. Reinecke, Hillebrandt & Niemeyer 2002; Gamezo et al. 2003; Röpke & Hillebrandt 2005; Röpke & Niemeyer 2007) are the state-of-the-art and have shown that 3D effects are essential to properly simulate the instabilities and turbulence effects which drive the thermonuclear combustion. Furthermore they show that ejecta asymmetries can arise, either by hydrodynamical instabilities during the burning phase or an asymmetric ignition (Höflich & Stein 2002; Kuhlen, Woosley & Glatzmaier 2006).

However these simulations – which give velocities, densities and composition of the explosion ejecta – are not directly comparable to observations of real SNe Ia. For that purpose synthetic spectra and light curves must be obtained by radiative transfer calculations. This requires a solution of the multi-line transfer problem in expanding media where the opacity is dominated by the wealth of lines associated with the iron group elements which were synthesised in the thermonuclear explosion. Many 1D studies have addressed this problem in the past either assuming pure resonance scattering (e.g. Branch et al. 1982, 1983; Mazzali & Lucy 1993) or pure absorption (e.g. Jeffery et al. 1992) in the lines. Lucy (1999b) introduced an approximate treatment of line fluorescence. But that work is still in 1D as are the studies done with the general-purpose radiation transport code PHOENIX (e.g. Lentz et al. 2001). Recently following Lucy (2005), Kasen, Thomas & Nugent (2006) described a 3D time-dependent radiative transfer code which is capable of treating line fluorescence in an approximate way (similar to Lucy 1999b; Pinto & Eastman 2000).

Such studies have shown that to address the complexity of the hydrodynamic explosion models a 3D treatment of radiative transfer which simulates the γ-deposition and spectrum formation in detail is needed. In particular, a careful treatment of the ionisation balance and a proper simulation of the redistribution of flux by line fluorescence [crucial for the near-infrared light curves, see Kasen (2006)] is essential. Here we present a new Monte Carlo code (ARTIS, Applied Radiative Transfer In Supernovae) which (based on the approach of Lucy 2002, 2003, 2005) solves the time-dependent 3D radiative transfer problem in chemically inhomogeneous models of supernova ejecta from first principles using a generalised treatment of line formation and prioritising a detailed treatment of ionisation. The radiative transfer calculation is parameter-free, depending only on the input model and atomic data, giving a maximum of predictive power for a given hydro model. Details of our code are given in Section 2.

In Section 3 we use this code to calculate model spectra and light curves for the well-studied 1D deflagration model W7 (Nomoto et al. 1984) and compare them to observations and earlier synthetic results in order to test our code. We also investigate the influence of completeness of atomic data. Finally, in Section 4, line-of-sight dependent spectra and light curves for an ellipsoidal toy model are calculated to demonstrate the multi-dimensional capabilities of our code and study the effect of large scale asymmetries of the ejecta, before we draw conclusions in Section 5.

2 METHOD

Monte Carlo methods have been widely applied to model astrophysical radiative transfer in expanding media (e.g. Abbott & Lucy 1985 and Lucy & Abbott 1993 for winds of massive stars and Mazzali & Lucy 1993 for the expanding envelopes of supernovae). This is mainly due to the ease with which they address the multi-line transfer problem – a single photon can interact with many spectral lines due to the progressive redshift it experiences in the co-moving frame while it travels through the expanding envelope. Monte Carlo methods are also readily extended to multi-dimensional problems (see e.g. Kasen et al. 2006 and Maeda, Mazzali & Nomoto 2006) and easy to parallelise, allowing the exploitation of massively parallel super computers.

As the typical expansion velocities in supernova envelopes ($\lesssim 30\,000\,\mathrm{km\,s^{-1}}$) imply large velocity gradients, the physical properties of the envelope will not change significantly within the resonance region of a spectral line (Doppler velocity $v_\mathrm{D} \sim 5\,\mathrm{km\,s^{-1}}$) and we adopt the Sobolev approximation and consider that line absorption of photons takes place only at a particular point of resonance. This simplifies the problem significantly and is a fundamental assumption of our study. For a detailed description of the Sobolev approximation see e.g. Mihalas (1978) or Lamers & Cassinelli (1999).

The second fundamental assumption we make is that of homologous expansion, thereby decoupling the radiative transfer from the hydrodynamic evolution of the ejecta. This applies if the ejecta are in free expansion, i.e. their kinetic energy density dominates the gravitational and internal energy densities. For SNe Ia this is achieved less than a minute after the explosion (e.g. Röpke 2005). Thus it should be an excellent approximation for our radiative transfer calculations which are usually started at ~ 2 days. In homologous expansion the velocity v of the ejecta at a particular position r is always proportional to the position, $v = r/t$ with t being the time since explosion.

2.1 Monte Carlo radiative transfer

We extended the 3D Monte Carlo radiative transfer code introduced by Sim (2007) to a non-grey opacity treatment following the scheme outlined in a series of papers by Lucy (2002, 2003, 2005). This scheme is based on the artificial division of the radiation field into indivisible energy packets as Monte Carlo quanta, rather than Nature's quantisation of radiation. This has two major advantages: first it keeps the code simple as packet histories can be followed one-by-one, avoiding the need to follow multiple packets in e.g. recombination cascades. Second it ensures rapid convergence to an accurate temperature stratification by imposing the constraint of energy conservation in the co-moving frame (Lucy 1999a).

In the following we outline the operation of the code with reference to the flow chart shown in Figure 1 and discuss the relevant physical processes, giving detail only where

we deviate from the formulations used by Lucy (2002, 2003, 2005). The basic transfer calculations are carried out in the rest frame (rf, quantities always denoted unprimed) so that an energy packet's trajectory at time t is described by its position $\boldsymbol{r}(t)$ and direction $\boldsymbol{\mu}(t)$. For interactions with matter we transform to the local co-moving frame (cmf, quantities denoted with prime).

2.1.1 Setting up the computational domain

To avoid any symmetry assumptions and keep the code simple, we map the explosion ejecta to a 3D Cartesian grid with origin at the centre-of-mass of the supernova and containing I^3 cubic cells. The grid expands with time to follow the evolution of the ejecta. Physical variables are assumed not to vary spatially within the grid cells. As input we take densities $\rho_i(t)$, velocities $v_i(t)$ and composition $X_{i,k}(t)$ from explosion models specified for the phase of homologous expansion and map these for a time t_0 onto the grid. t_0 and all time specifications in the following indicate the time since explosion, unless otherwise noted.

We then follow the expansion of the ejecta for N time steps up to time t_N by expanding the individual grid cells continuously. The time steps (t_n,t_{n+1}) are spaced logarithmically and thermodynamic quantities in a cell such as densities, temperatures and atom/ion populations are kept fixed during a time step n at the value they have for $t_{n+0.5}$.

2.1.2 Energy deposition

SNe Ia light curves are primarily powered by the radioactive decays of ^{56}Ni$\rightarrow^{56}$Co and ^{56}Co$\rightarrow^{56}$Fe (Truran, Arnett & Cameron 1967; Colgate & McKee 1969) giving rise to the emission of a spectrum of γ-photons associated with their transitions (Ambwani & Sutherland 1988). Out of the total energies, $E_{\rm Ni}$ and $E_{\rm Co}$ emitted per decay of ^{56}Ni and ^{56}Co, we determine the total γ-ray energy emitted in the decay chain for $t \rightarrow \infty$

$$E_{\rm tot} = (E_{\rm Ni} + E_{\rm Co})M_{\rm Ni}/m_{\rm Ni}. \quad (1)$$

$M_{\rm Ni}$ is the initial mass of ^{56}Ni synthesised in the explosion and $m_{\rm Ni}$ the mass of the ^{56}Ni atom.

Following Lucy (2005), this energy is quantised into $\mathcal{N} = E_{\rm tot}/\epsilon_0$ identical energy packets of cmf energy ϵ_0 which we call "pellets" in the following. These pellets are distributed on the grid according to the initial ^{56}Ni distribution and follow the homologous expansion until they decay. Decay times are sampled randomly according to the ^{56}Ni$\rightarrow^{56}$Co$\rightarrow^{56}$Fe decay chain with pellets assigned to represent either the ^{56}Ni or ^{56}Co decay.

Upon decay, a pellet transforms to a single γ-packet representing a bundle of monochromatic γ-radiation with cmf energy ϵ_0 and a cmf photon energy E'_γ which is randomly sampled from the γ-lines in the appropriate decay of the sequence ^{56}Ni$\rightarrow^{56}$Co $\rightarrow^{56}$Fe. The γ-packet's direction ($\boldsymbol{\mu'}$) in the cmf is sampled randomly assuming isotropic emission.

2.1.3 Propagation of γ-packets

The γ-packets are propagated through the ejecta in the rest frame of the grid until either (i) they leave the grid, (ii) the current time step finishes or (iii) they interact with matter. Computing the distances to all possible events along the packet trajectory, we select the event which is reached first [see Lucy (2005) for details]. In the first case the γ-packet is flagged inactive and the calculation proceeds to the next active packet. In the second case we save the rf data string ($\boldsymbol{r}$, t, $\boldsymbol{\mu}$, ϵ, E_γ) for the following time step and continue with the next active packet.

For the third case we consider Compton scattering by free and bound electrons, photoelectric absorption and pair production as possible physical processes, the last being only available for γ-packets with energy $E > 2m_{\rm e}c^2$. For details see again Lucy (2005) and Equation 1 of Sim & Mazzali (2008) for the adopted photoabsorption cross-section. Which of the processes happens is determined randomly according to their absorption and scattering coefficients.

In the case of a photoelectric absorption, the γ-packet energy is deposited as thermal kinetic energy. In the framework of this code, this is described by a transformation of the γ-packet into a so-called k-packet of equal cmf energy. The treatment of k-packets is described in section 2.1.4.

As our energy packets are indivisible, the treatment of Compton scattering and pair production, where the photon energy is distributed to two particles, is slightly more complex. Following again Lucy (2005), for Compton scattering the γ-packet is either scattered and continues as a γ-packet of the same cmf energy as the incident packet or it is transformed into a non-thermal e^--packet. e^--packets are assumed to thermalise and are instantaneously transformed into k-packets. For pair production we either create e^+- or e^--packets. Assuming in situ annihilation, for an incident γ-packet of cmf photon energy E'_γ a fraction of $2m_{\rm e}c^2/E'_\gamma$ (represented by the e^+-packets) is released in form of γ-rays at 0.511 MeV when the positron annihilates. The remainder (representing the kinetic energy of the electrons and positrons) goes directly to the thermal pool.

2.1.4 Treatment of thermal kinetic energy

Neglecting energy storage in the ejecta gas, thermal kinetic energy converts instantaneously (i.e. without propagating) into ultraviolet-optical-infrared (*UVOIR*) radiation. This happens either directly via continuum emission by free-free or free-bound processes or indirectly by collisional excitations/ionisations of the gas and subsequent radiative de-excitations/recombinations. In our framework, this means either transforming a k-packet into an r-packet – representing a monochromatic energy packet of *UVOIR* radiation (for details see Section 2.1.6) – or into a packet of atomic internal energy, which we call i-packets. Details of the latter will be discussed in the next section.

Which of the processes happens depends on the cooling rate associated with the particular process and is sampled randomly. For the free-bound cooling rate we consider only spontaneous recombination since stimulated recombination is treated as negative photoionisation and, as such, is taken into account in the creation of k-packets.

From sampling the cooling rates, we know in which free-bound continuum (specified by level i of ion j of element k) to emit or whether free-free emission was selected. In both cases the r-packet's direction in the cmf $\boldsymbol{\mu'}$ is determined according to isotropic emission and the cmf energy

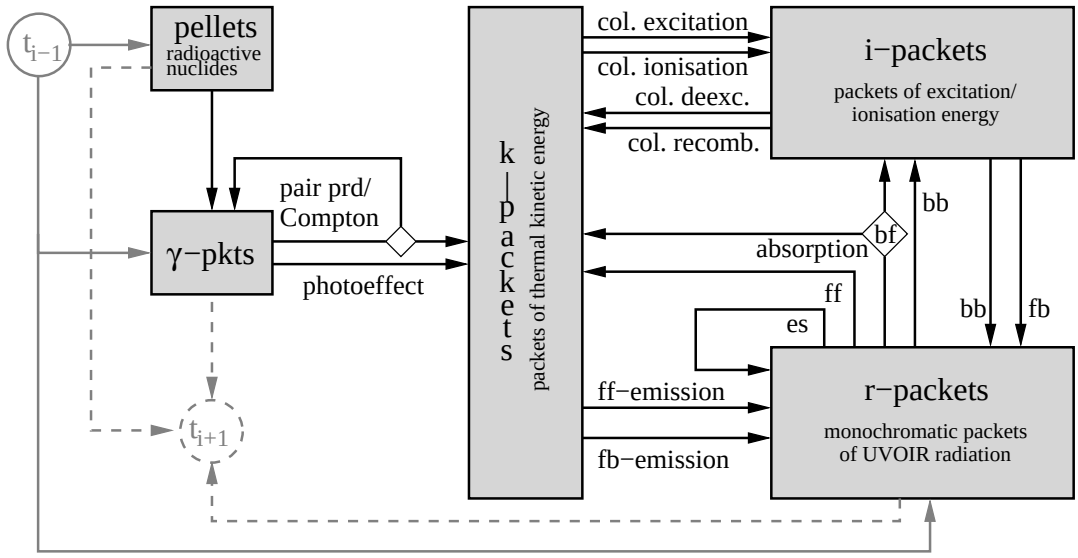

Figure 1. Flow chart outlining the mode of operation of the code. For discussion see text.

ϵ' of the generating packet is conserved. After transforming these quantities into the rf together with the packet's position ($\boldsymbol{r}$), we must determine the r-packet photon frequency before continuing its propagation through the grid.

For free-free emission the frequency is determined from

$$\int_{\nu}^{\infty} j^{\mathrm{ff}}(\nu')\,\mathrm{d}\nu' = z\int_{0}^{\infty} j^{\mathrm{ff}}(\nu')\,\mathrm{d}\nu' \tag{2}$$

with z a random number in $]0,1[$ and $j^{\mathrm{ff}}(\nu) \propto \exp^{-h\nu/kT_{\mathrm{e}}}$ (we neglect the frequency dependence of the velocity-averaged Gaunt factor). For free-bound emission we use

$$\int_{\nu}^{\infty} j^{\mathrm{fb}}_{i,j,k}(\nu')\,\mathrm{d}\nu' = z\int_{\nu_{i,j,k}}^{\infty} j^{\mathrm{fb}}_{i,j,k}(\nu')\,\mathrm{d}\nu' \tag{3}$$

with z a random number in $]0,1]$ and where $\nu_{i,j,k}$ is the edge frequency of the continuum. The emissivity $j^{\mathrm{fb}}_{i,j,k}(\nu)$ for spontaneous recombination by that continuum is given by Equation 23 of Lucy (2003).

In principle we want to only release thermal energy when transforming a k-packet to an r-packet. However in emitting a bound-free photon at frequency ν, a fraction $\nu_{i,j,k}/\nu$ of the packet energy is drawn from the ionisation/excitation energy pool. The machinery described in the next section ensures that this is balanced by the amount of thermal energy which is released by recombination processes in our treatment of atomic internal energy (see also Lucy 2003).

2.1.5 Treatment of atomic internal energy

We treat atomic internal energy using the macro-atom approach of Lucy (2002, 2003) which is based on an interpretation of statistical equilibrium in terms of macroscopic energy flow rates. For Monte Carlo methods this is an improvement over earlier work in 1D (e.g. Mazzali & Lucy 1993; Lucy 1999b) or in 3D (Kasen et al. 2006). We stress that the macro-atom approach allows for a fully general treatment of radiation/matter interactions in statistical equilibrium, including true absorption, scattering and fluorescence.

Whenever a packet is converted to atomic internal energy (i-packet), we assign it to a macro-atom state (see Lucy 2002 for relevant definitions). The ejecta gas can be excited/ionised either collisionally, represented by a k-packet to i-packet transition (see last section) or radiatively by *UVOIR* radiation, represented by an r-packet to i-packet transition. Non-thermal excitations by fast electrons and γ-rays are not currently taken into account but the method could be extended to include them in due course.

For k-packet to i-packet transitions, the macro-atom state is determined by sampling the cooling rates for collisional excitation/ionisation, which are calculated in the van Regemorter and Seaton approximations (Mihalas 1978). For r-packet to i-packet transitions, the absorption process identifies the appropriate macro-atom state directly. Details of the treatment of r-packets are given in Section 2.1.6.

We do not take into account energy storage in the ejecta gas but assume i-packets convert instantaneously back into k- or r-packets. For that purpose we calculate rates for all transitions which connect an activated state to other macro-atom states or which allow the macro-atom to deactivate, i.e. transform the internal atomic energy back to either thermal kinetic (k-packet) or radiative (r-packet) energy. From all these transitions we randomly select one by sampling the probabilities which are computed following Lucy (2003). If it is a macro-atom internal jump we reset the i-packet macro-atom state and continue this procedure until we select a deactivating process.

During deactivations we conserve the cmf energy of the packet to enforce radiative equilibrium. In the case of a collisional deactivation the i-packet is just transformed into a k-packet. In case of radiative deexcitation/recombination we transform the i-packet into an r-packet and emit it isotropically in the cmf. Finally we need to assign a photon frequency to the r-packet. For a radiative deexcitation this is given by the frequency of the associated line transition in the cmf. In the case of a radiative recombination, we again sample the emissivity for the free-bound emission (Equation

3). Note that we thereby emit both ionisation and thermal energy, as we do it in the case of free-bound cooling.

2.1.6 Propagation of UVOIR radiation

r-packets representing monochromatic energy packets of *UVOIR* radiation are propagated through the ejecta from their first emission by any of the above processes until (i) they leave the grid, (ii) the current time step finishes or (iii) they interact with matter. In the zeroth time step we also have radiation which comes from pellets which decayed before t_0. We assume that the ejecta are optically thick at these early times such that the radiation is trapped and local thermodynamic equilibrium (LTE) is a good approximation. Therefore we emit these packets isotropically at the position the pellets would have at t_0 and assign them frequencies according to a black-body distribution at the local kinetic temperature T_e.

We follow the packets along their trajectory until they are stopped by the first event which occurs. For (i) and (ii) this is a simple geometrical problem. For case (iii) it requires calculating the distance to a randomly sampled optical depth $\tau_\mathrm{r} = -\ln z$ with $z \in]0,1]$, as described by Mazzali & Lucy (1993). First the trajectory point at which the photon comes into resonance with the next spectral line of the line list is calculated in the Sobolev approximation. If the continuum optical depth accumulated up to that point is bigger than the random optical depth, the travelled distance ds is calculated from the continuum opacity (κ_cont) from $\kappa_\mathrm{cont}\mathrm{d}s = \tau_\mathrm{r}$ and a continuum absorption occurs. If the sum of continuum and line optical depth is bigger than the random optical depth, ds is given by the distance to the resonance point and a line event occurs. Otherwise we calculate the distance to the next spectral line with which the photon comes into resonance and repeat the procedure.

According to the chosen event, the packet properties are now updated. For case (i), the r-packet is flagged inactive and we proceed to the next active packet. For case (ii), we save the actual rf data string ($\boldsymbol{r}$, t, $\boldsymbol{\mu}$, ϵ, ν) for the following time step and continue with the next active packet. For case (iii), we change the packet type according to the process which terminated the packet flight. For a line absorption, we convert the r-packet into an i-packet and set it to the corresponding macro-atom target state and the macro-atom machinery (Section 2.1.5) determines its fate.

For a continuum event, we first decide whether it was Thomson scattering, free-free absorption or bound-free absorption by randomly sampling their absorption coefficients. Thomson scattering, which we assume to be coherent and isotropic, changes neither the packet type, nor the cmf frequency of the packet. Thus, Thomson scattering amounts to isotropic reemission of the r-packet in the local cmf. Free-free absorption transforms the absorbed radiative energy completely into thermal kinetic energy, i.e. converts the r-packet into a k-packet.

Bound-free absorption is more complicated since it contributes both to atomic internal energy and thermal kinetic energy. After randomly selecting one specific continuum according to its absorption coefficient, we follow Lucy in forcing a conversion to either a single k- or i-packet. For an r-packet absorbed with frequency ν by a continuum with edge frequency $\nu_{i,j,k}$, a fraction $\nu_{i,j,k}/\nu$ of its energy is converted to atomic internal energy and the rest to thermal kinetic energy. To account for this, we convert the packet to an i-packet with probability $\nu_{i,j,k}/\nu$, setting it to the corresponding macro-atom state, and to a k-packet otherwise.

To speed up the calculations, we introduced an optional initial grey approximation in the code. Controlled by two input parameters $\tau_\mathrm{Th,min}$ and N_grey, the propagation of *UVOIR* radiation in cells which have a Thomson optical depth $\tau_\mathrm{Th} > \tau_\mathrm{Th,min}$ is performed including Thomson scattering as the only source of opacity. If τ_Th falls below $\tau_\mathrm{Th,min}$, and for all time steps later than N_grey, we switch back to the non-grey treatment. This speeds up the initial phase of a calculation by a factor of ~ 10, since much of the ejecta are still rather dense and photons cannot propagate. With a good selection of $\tau_\mathrm{Th,min}$ and N_grey the differences in spectra and light curves from a fully non-grey calculation are negligible.

2.1.7 Extraction of spectra and light curves

When the simulation has finished, we extract the spectral evolution by binning the escaping r-packets in frequency, time and direction of escape, accounting for light travel-time effects. Colour light curves are extracted from the spectral evolution by integrating the spectra over the appropriate filter functions (Bessell & Brett 1988; Bessell 1990). *UVOIR* bolometric light curves are extracted by binning the escaping r-packets by time and angle. Similarly γ-ray spectra and light curves can be obtained from the γ-packets.

Using the formal integral method developed by Lucy (1999b) to extract spectra and light curves would substantially reduce the Monte Carlo noise. However, the need to store line and continuum source functions in all grid cells for all lines and continua included in the simulation (typically $10^5 \ldots 10^7$) causes the simulation memory requirements to be so high that this method becomes computationally prohibitive, even with current state-of-the-art super computers for 3D grids. Therefore all results presented here have been obtained using the direct binning approach.

2.2 Plasma conditions

To calculate opacities we need to know atomic level populations which in turn depend on the radiation field. In principle, these could be extracted exactly out of our simulation, but it is computationally restrictive to record the complete set of level-by-level radiative rates for every grid cell which would be required to do this. Therefore we use an approximate model for the radiation field and for excitation and ionisation conditions. Two different descriptions have been implemented in our code. The first parameterises the ionisation balance in a simple one-temperature description using the Saha formula. This is less demanding of computational resources but also less accurate than our second which treats ionisation in detail and simultaneously solves the thermal balance equation.

2.2.1 Radiation field models

Following Lucy (2003), the zeroth moment of the radiation field in a grid cell can be reconstructed from the Monte Carlo packets using the estimator

$$J_\nu \mathrm{d}\nu = \frac{1}{4\pi \Delta t V} \sum_{\mathrm{d}\nu} \epsilon_\nu^{\mathrm{cmf}} \mathrm{d}s \tag{4}$$

where Δt is the length of the time step, V the grid cell volume, $\mathrm{d}s$ the trajectory length within the grid cell and $\epsilon_\nu^{\mathrm{cmf}}$ the packet energy in the cmf. The summation runs over all trajectory segments $\mathrm{d}s$ in V for which the packet frequency $\nu \in [\nu, \nu + \mathrm{d}\nu]$.

As discussed above, we do not use this general description directly but parameterise the radiation field. For the simple one-temperature description of ionisation, the radiation field is parameterised as a black body,

$$J_\nu = B_\nu \left(T_{\mathrm{J}}\right) \tag{5}$$

at a temperature T_{J} corresponding to the local energy density of the radiation field ($B_\nu(T)$ is the Planck function). The parameter T_{J} can be extracted by equating the frequency integrated estimator $\langle J \rangle \equiv \int_0^\infty J_\nu \, \mathrm{d}\nu$ (where J_ν is given by Equation 4) with the Stefan-Boltzmann law

$$T_{\mathrm{J}} = \left(\pi \langle J \rangle / \sigma\right)^{1/4}. \tag{6}$$

In our simple ionisation treatment, we also equate the kinetic temperature $T_{\mathrm{e}} = T_{\mathrm{J}}$.

For the detailed ionisation treatment we parameterise the radiation field using a nebular approximation

$$J_\nu = W B_\nu \left(T_{\mathrm{R}}\right), \tag{7}$$

with the radiation temperature T_{R} and the dilution factor W as parameters. T_{R} is chosen such that the mean-intensity weighted mean frequency of the radiation field $\langle \nu \rangle \equiv \int_0^\infty \nu J_\nu \, \mathrm{d}\nu / \int_0^\infty J_\nu \, \mathrm{d}\nu$ matches that of a blackbody at T_{R}. Following Mazzali & Lucy (1993) T_{R} and W can be extracted from $\langle J \rangle$ and $\langle \nu \rangle$ by

$$W = \frac{\pi \langle J \rangle}{\sigma T_{\mathrm{R}}^4} \qquad \text{and} \qquad T_{\mathrm{R}} = \frac{h \langle \nu \rangle}{x k_{\mathrm{B}}} \tag{8}$$

with $x = 360 \cdot \zeta\left(5\right) / \pi^4$ and $\zeta\left(x\right)$ being Riemann's ζ-function. T_{J} remains defined as in the simple ionisation treatment (implying $T_{\mathrm{J}} = W^{1/4} T_{\mathrm{R}}$ from Equation 6).

2.2.2 Excitation and ionisation

Independent of the ionisation description used, we apply the Boltzmann formula evaluated at T_{J}

$$\frac{n_{i,j,k}}{n_{0,j,k}} = \frac{g_{i,j,k}}{g_{0,j,k}} \exp\left(-\frac{\epsilon_{i,j,k} - \epsilon_{0,j,k}}{k_{\mathrm{B}} T_{\mathrm{J}}}\right) \tag{9}$$

to calculate the population $n_{i,j,k}$ of a level i of ion j of element k relative to the ion ground state population $n_{0,j,k}$. $g_{i,j,k}$ and $\epsilon_{i,j,k}$ are statistical weights and energies of the corresponding levels.

Assuming ionisation equilibrium in a radiation dominated environment[1], we require

$$\sum_{i=0}^{\mathcal{N}_{j,k}} n_{i,j,k} \gamma_{i,j,k} = n_e N_{j+1,k} \sum_{i=0}^{\mathcal{N}_{j,k}} \left(\alpha_{i,j,k}^{\mathrm{sp}} + \alpha_{i,j,k}^{\mathrm{st}}\right) \tag{10}$$

where $\mathcal{N}_{j,k}$ is the number of levels associated with ion j of element k, and n_{e} the density of free electrons. $\gamma_{i,j,k}$ denotes the photoionisation rate coefficient from a bound level i, j, k and $\alpha_{i,j,k}^{\mathrm{sp}}$ is the rate coefficient for spontaneous recombination from the $(j+1)$-th ion to the bound state i, j, k (see e.g. Mihalas 1978). In our simple one-temperature ionisation treatment this reduces to the Saha equation

$$\frac{N_{j,k}}{N_{j+1,k} n_e} = \frac{U_{j,k}}{U_{j+1,k}} \frac{C}{T_{\mathrm{e}}^{3/2}} \exp\left(\frac{\epsilon_{0,j+1,k} - \epsilon_{0,j,k}}{k_{\mathrm{B}} T_{\mathrm{e}}}\right) \tag{11}$$

where

$$C = \frac{1}{2}\left(\frac{h^2}{2\pi m_{\mathrm{e}} k_{\mathrm{B}}}\right)^{3/2} \tag{12}$$

and $U_{j,k}$ is the partition function of ion j of element k.

For the detailed ionisation treatment we neglect stimulated recombination, which is small compared to spontaneous recombination, and use the partition function together with

$$\Gamma_{j,k} \equiv \sum_{i=0}^{\mathcal{N}_{j,k}} \frac{n_{i,j,k} \gamma_{i,j,k}}{n_{0,j,k}} \qquad \text{and} \qquad A_{j,k}^{\mathrm{sp}} \equiv \sum_{i=0}^{\mathcal{N}_{j,k}} \alpha_{i,j,k}^{\mathrm{sp}} \tag{13}$$

to obtain the following ionisation formula from Equation 10

$$\frac{N_{j,k}}{N_{j+1,k} n_{\mathrm{e}}} = \frac{A_{j,k}^{\mathrm{sp}}}{\Gamma_{j,k}} \cdot \frac{U_{j,k}}{g_{0,j,k}} \tag{14}$$

Since $\alpha_{i,j,k}^{\mathrm{sp}}$ does not depend directly on the radiation field, we calculate $A_{j,k}$ by summing all the $\alpha_{i,j,k}^{\mathrm{sp}}$ of the ion j, k evaluated at the local kinetic temperature T_{e}.

In contrast, the photoionisation rate coefficients $\gamma_{i,j,k}$ depend directly on the radiation field and should be determined from volume-based Monte Carlo estimators for most accurate results. However, we cannot afford to store $\gamma_{i,j,k}$ for each bound-free continuum in every grid cell. Instead we derive $\gamma_{i,j,k}^*$ from an integration of the radiation field model (Equation 7) using the local values of T_{R} and W. Estimated in this way $\gamma_{i,j,k}^*$ is expected to be reliable for bound-free absorptions which lie around the peak of the radiation field. However, the radiation field model is inadequate at very blue frequencies where the spectrum is systematically affected by bound-free edges. Thus to track the effect of absorption continua on the radiation field, we record estimators $\gamma_{0,j,k}$ for the photoionisation rate coefficient of the ground level continua and use them to derive renormalisation coefficients $\zeta_{0,j,k} = \gamma_{0,j,k} / \gamma_{0,j,k}^*$. To obtain the $\gamma_{i,j,k}$ in $\Gamma_{j,k}$ of Equation 13 we renormalise all the integrated photoionisation rate coefficients via

$$\gamma_{i,j,k} = \zeta_{0,j',k'} \gamma_{i,j,k}^*, \tag{15}$$

[1] Currently we consider only photoionisation and radiative recombination. Temperatures in the recombination zones of iron group elements are sufficiently low that dielectronic recombination (calculated according to Shull & van Steenberg 1982) is small compared to radiative recombination. However we note that in high temperature environments it may become important, especially for intermediate mass elements. For more detailed studies our treatment could readily be extended to incorporate additional ionisation/recombination processes (including dielectronic recombination and non-thermal ionisation).

where we take the $\zeta_{0,j',k'}$-value from the ground level continuum which lies closest in edge frequency to the considered continuum (i.e., the one for level i,j,k). For continua redder than the reddest ground level continuum, ζ is set to 1.

For the zeroth time step, and also for cells treated in our initial grey approximation (see Section 2.1.6), we use the simple ionisation treatment. We also assume that at all times prior to our zeroth time step the ejecta are sufficiently optically thick, that all the radiation is trapped. Thus we calculate initial temperatures $T_{\rm e,0} = T_{\rm R,0} = T_{\rm J,0}$ for each grid cell from the energy released by the decay of ^{56}Ni in the cell prior to the midpoint of the zeroth time step. Since the trapping is not really perfect, it takes a few (typically ~ 5) time steps until the propagation of the energy packets washes out the effect of this boundary condition on temperatures and level/ion populations.

In practise this boundary condition primarily effects calculations using the detailed ionisation description. In this case, it is more important to have accurate level populations as errors can feed back to the thermal balance calculation. Thus we typically do the first ~ 10 time steps of a calculation in the simple ionisation treatment to obtain reliable initial conditions for the detailed ionisation treatment at all later times. Since our simple ionisation treatment reproduces LTE conditions we expect it to be a good approximation at early times when optical depths are high.

2.2.3 Thermal balance

In the detailed ionisation description, we also solve for the local kinetic temperature $T_{\rm e}$ in a grid cell by balancing the local heating $\mathcal{H}$ and cooling $\mathcal{C}$ rates. The heating rates are calculated from the previous time step using volume-based Monte Carlo estimators for the heating by γ-rays (see Lucy 2005) and free-free absorptions (see Lucy 2003) and event-based Monte Carlo estimators for the heating by collisional deexcitation/recombination.

We cannot afford to store a bound-free heating estimator for each continuum in every grid cell. Thus bound-free heating rates

$$\mathcal{H}^{\rm bf}_{i,j,k} = n_{i,j,k} h^{\rm bf}_{i,j,k} = n_{i,j,k} \left(\gamma^{\rm E}_{i,j,k} - \gamma_{i,j,k}\right) h\nu_{i,j,k}, \qquad (16)$$

(with $\gamma^{\rm E}_{i,j,k}$ the modified rate coefficient for photoionisation as defined by Lucy 2003) are not obtained directly from Monte Carlo estimators but from an integration of the radiation field model using the local values of $T_{\rm R}$ and W yielding $h^{\rm bf,*}_{i,j,k}$. As for the photoionisation rate coefficients (Section 2.2.2), we then use estimators $h^{\rm bf}_{0,j,k}$ for the bound-free heating coefficient of the ground level continua to derive renormalisation coefficients $\xi_{0,j,k} = h^{\rm bf}_{0,j,k}/h^{\rm bf,*}_{0,j,k}$. These are used to calculate the bound-free heating coefficients

$$h^{\rm bf}_{i,j,k} = \xi_{0,j',k'} h^{\rm bf,*}_{i,j,k} \qquad (17)$$

where we again take the $\xi_{0,j',k'}$ which lies closest in frequency to the considered continuum (i.e., the one for level i,j,k) to track the effect of absorption continua on the radiation field. Continua which are redder than the reddest ground-level continuum are not renormalised.

We include cooling by free-free and free-bound emission, collisional excitation/ionisation and adiabatic expansion. Since these cooling rates do not depend on the radiation field directly, they are calculated from the current set of level populations and $T_{\rm e}$ as described in Lucy (2003). The adiabatic cooling rate is given by

$$\mathcal{C}^{\rm ad} = p\frac{{\rm d}V}{V} \qquad (18)$$

with p the gas pressure and V the volume of the grid cell.

Balancing the heating and cooling rates on a temperature interval $[T_{\rm min}, T_{\rm max}]$ with $T_{\rm min} = 3500\,{\rm K}$ and $T_{\rm max} = 1.4\cdot10^5$ K in our simulations, leads to a new value of $T_{\rm e}$. For cells in which the heating and cooling rates cannot be balanced on this interval, $T_{\rm e}$ is set to the upper/lower boundary value if the heating/cooling rates dominate. The same temperature limits apply to $T_{\rm J}$ and $T_{\rm R}$. $T_{\rm max}$ is chosen such that it will be only reached at the very earliest times in the inner iron-rich core where the opacity is so high that the radiation is trapped (actually for the simulations described in this paper $T_{\rm max}$ was never reached). $T_{\rm min}$ will be reached at late times but only in layers which are sufficiently optically thin that they have no strong influence on the spectrum formation.

Assuming that time steps are short enough and the radiation field does not depend strongly on the evolution of $T_{\rm e}$ we use the obtained value for $T_{\rm e}$ and the same Monte Carlo estimators as before to re-solve for the populations and then for thermal balance again. Repeating this iteratively we reach a converged solution for $T_{\rm e}$ and the ionisation state. This iteration can be extended to an outer loop in which the Monte Carlo simulation is also repeated. Kasen et al. (2006, Section 3.4) showed that, even from crude initial conditions, such an iteration converges very rapidly. By using short time steps and initial thermodynamic quantities from the previous time step, we found that such an outer iteration of the Monte Carlo experiment does not affect the results strongly. Thus we do not iterate on the Monte Carlo simulation for each time step in the simulations described below (however the option to do so remains in the code).

2.3 Model atoms

The most important opacity source in supernova envelopes is the wealth of bound-bound line transitions associated with the iron group elements synthesised by the thermonuclear explosion. Thus an extensive line list which covers all the important species is needed. We restrict our atomic data to the lowest five ionisation stages of elements up to Zn, neglecting H, Li, Be and B. To study the sensitivity to the choice of atomic data, we use two datasets which are based on the $\sim 5{\cdot}10^5$ lines of Kurucz & Bell (1995) (CD23) and the more modern theoretical atomic data computed by Kurucz (2006)[2] which are far more comprehensive but still not complete. For example this dataset contains $\sim 3.5\cdot10^7$ lines associated with the important second and third ions of Fe, Co and Ni compared to only $\sim 1.2\cdot10^5$ in CD23.

Since it is computationally too demanding to use all of the lines in a dataset, when constructing model atoms we apply cuts in $\log(gf)$ to reduce the number of lines. From the comprehensive dataset we take only the lines of Fe II, Fe III, Co II, Co III, Ni II and Ni III, the most important

[2] Available at `http://kurucz.harvard.edu/atoms.html`.

Table 1. Model atoms used in the calculations. Source A is Kurucz & Bell (1995), Source B Kurucz (2006).

Model name	Source	log(gf)	Levels	Lines (total)
cd23_gf-2	A	-2	18237	$1.4 \cdot 10^5$
cd23_gf-3	A	-3	18815	$2.5 \cdot 10^5$
cd23_gf-5	A	-5	19472	$4.1 \cdot 10^5$
cd23_gf-20	A	-20	21100	$4.7 \cdot 10^5$
big_gf-3	B (Fe II–III)	-3	41829	$3.5 \cdot 10^6$
	B (Co II–III)	-3	31816	
	B (Ni II–III)	-3	24853	
	A (other)	-3	16616	
big_gf-4	B (Fe II–III)	-4	47141	$8.2 \cdot 10^6$
	B (Co II–III)	-4	36442	
	B (Ni II–III)	-4	28022	
	A (other)	-4	17523	

species in the spectrum forming region, and continue to use the data of CD23 for all the other species and remaining ions of Fe, Co and Ni. In this way, we created a set of model atoms (summarised in Table 1) which are used in the following calculations.

Bound-free cross sections are obtained from the fits by Verner & Yakovlev (1995) or Verner et al. (1996) where available. A hydrogenic approximation is adopted for excited configurations.

3 APPLICATION TO THE W7 MODEL

As a first test we calculate the spectral evolution for the one-dimensional deflagration model W7 (Nomoto et al. 1984; Thielemann, Nomoto & Yokoi 1986) which has already been investigated in several other radiative transfer studies (e.g. Jeffery et al. 1992; Höflich 1995; Nugent et al. 1997; Lentz et al. 2001; Salvo et al. 2001; Baron et al. 2006; Kasen et al. 2006) and is found to be in good overall agreement with observations.

Our calculations use $5 \cdot 10^6$ energy packets to follow the spectral evolution over 100 time steps from 2 to 80 days after explosion ($\Delta \log(t) \sim 0.037$) and were performed on a 50^3 grid using the cd23_gf-5 model atom (see Table 1 for details) with our detailed ionisation treatment. The first 10 time steps have been calculated in the simple ionisation treatment to obtain reliable initial values (see the discussion in Section 2.2.2). To save computational time we make use of our initial grey approximation setting $\tau_{\mathrm{Th,min}} = 15$ and $N_{\mathrm{grey}} = 40$.

Figure 2 shows the 2500 to 10 000 Å spectra for 15, 22 and 44 days after explosion, corresponding to -5, +2 and +24 days relative to B band maximum. The colour coding shows the element associated with the last line emission of escaping photons, giving an indication of the elements responsible for spectral features (absorption features of individually strong lines can be identified in the plot from their associated P Cyg emission). The contribution of photons which escaped after a bound-free or free-free emission to the total flux is negligible ($< 10^{-3}$) and not shown. The most striking individual features are the Ca II near-infrared (NIR) triplet at $\sim$ 8600 Å and the characteristic Si II line at 6355 Å which is clearly visible around maximum light. While the outer layers, which are dominated by intermediate mass elements, are optically thick, the spectra are dominated by

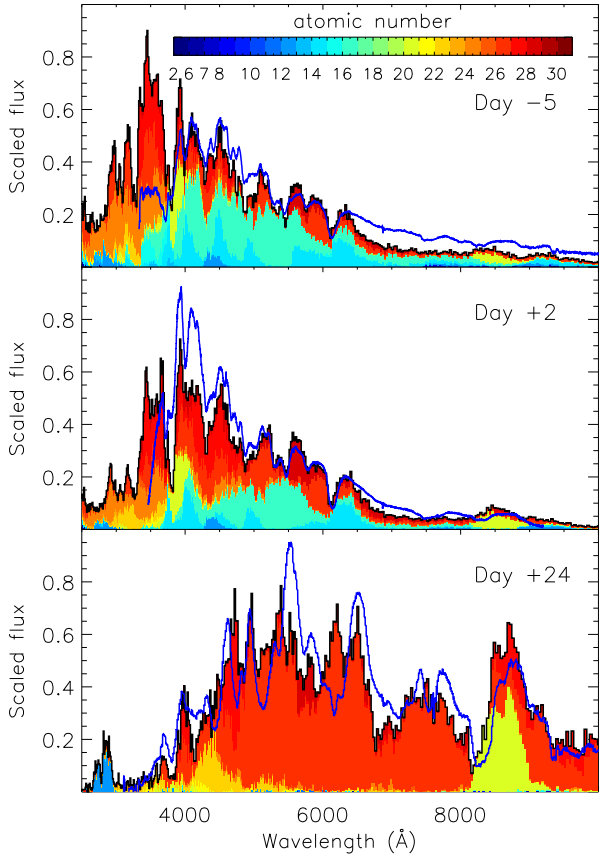

Figure 2. Spectra for the W7 explosion model at 5 days before and 2 and 24 days after maximum light in B band (from top to bottom) calculated using the detailed ionisation description and atomic dataset cd23_gf-5. Overplotted in blue are the observed spectra of SN 1994D for comparison (no redshift and extinction corrections have been applied). The colour coding shows the element associated with the last line emission of escaping photons. Atomic numbers in the colour legend are associated with the colour right to the number centre.

these elements. Around maximum light the outer layers become optically thin and the spectra start to be dominated by Fe group elements which completely take over at later times. Only individual strong lines of the lower mass elements (e.g. the Ca II NIR triplet) persist.

Overplotted with our synthetic spectra are observations of SN 1994D (Patat et al. 1996) for the corresponding epochs. Given that the W7 model has not been tuned to any particular supernova, the agreement of our model spectra with the observed ones is good. We reproduce the main spectral features, e.g. the Si II line and the Ca II NIR triplet, as well as the overall flux distribution. However there are obvious differences: at early times our model spectra have a strong excess in the UV flux below 4000 Å where Fe II, Fe III, Co III and Co IV dominate the spectrum formation. At late times we obtain emission in Fe II at $\sim$ 6050 Å where the data shows an absorption feature. Model spectra calculated for W7 by Kasen et al. (2006) show the same discrepancies compared to SN 1994D. This could be an indication

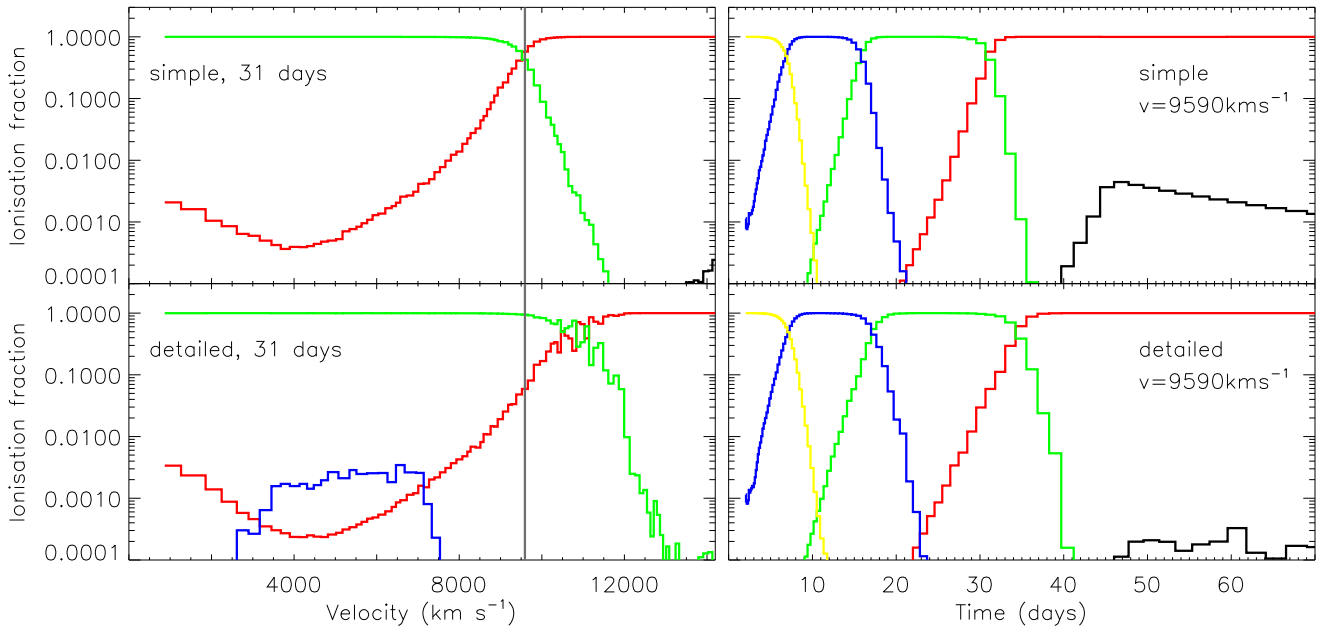

Figure 3. The left panels show the radial ionisation structure of Fe in the W7 explosion model at 31 days after the explosion obtained with the simple (top) and detailed ionisation treatment (bottom) and model atom cd23_gf-5. Black/red/green/blue/yellow lines represent Fe I/II/III/IV/V. The outer layers of the model, which consist only of unburned material and extend up to 22 800 km s^{-1}, are not shown. The right panels show the time evolution of the Fe ionisation structure at a velocity of 9590 km s^{-1} (indicated by the grey vertical line in the left panels) from 2 to 70 days for the two different ionisation treatments.

that some details of the explosion model would need to be changed to obtain better agreement with SN 1994D.

3.1 Simple versus detailed ionisation treatment

In the following we investigate how the two different ionisation treatments (see Section 2.2.2) which are implemented in our code affect the spectral evolution of a given explosion model. Therefore we also followed the spectral evolution of the W7 model using the cd23_gf-5 atomic data from 2 to 80 days after the explosion using the simple ionisation treatment.

Since differences in the spectral evolution must originate from the different ionisation treatment, we compare ionisation fractions from our different simulations in Figure 3. We focus on Fe since the iron group elements, which have similar ionisation structure to each other, dominate the spectra for the relevant epochs. The left panels of Figure 3 show the ionisation fractions as a function of radial velocity at 31 days after the explosion for the simple and detailed ionisation treatment. The right panels show the same ionisation fractions as a function of time at a radial velocity of 9590 km s^{-1}, which is marked by the grey vertical line in the left panels. This is the velocity at which the iron group mass fraction of the ejecta drops to 0.5 and thus is around the outer velocity of the iron-rich inner core.

From the left panels we see that, using the detailed ionisation treatment, the ejecta are more highly ionised at higher radial velocities. The right panels show that, with the detailed ionisation treatment, the ejecta also stay more highly ionised for a longer time at a given radius and never recombine as fully as with the simple ionisation treatment at late times. In the simple ionisation treatment, the ionisation is determined only by the energy density of the radiation field calculated from the r-packets. In the detailed ionisation treatment, the frequency distribution of the calculated radiation field has an important effect. $T_{\rm R} > T_{\rm J}$ and $W < 1$ (see Equations 6 – 8) with $T_{\rm R}$ and W departing more strongly from $T_{\rm J}$ and 1, respectively, with increasing time and decreasing ejecta density and opacity. Thus, there tend to be more high-energy ionising photons than suggested by the radiation field model of the simple ionisation treatment. This gives rise to higher ionisation states, particularly for later times. This is illustrated in Figure 4 which shows the time evolution of the radiation temperature $T_{\rm R}$ and the temperature $T_{\rm J}$ corresponding to the energy density of the radiation field at a radial velocity of 9590 km s^{-1}. While $T_{\rm J}$ drops similarly for the simple and detailed ionisation treatment, $T_{\rm R}$ for the detailed ionisation treatment stays significantly hotter from 20 days on.

$T_{\rm e}$ shows a similar decline and stays somewhat below $T_{\rm R}$ up to about maximum light (note that at very early times, prior to $\sim$ 10 days, this region is dominated by Fe V for which line transitions were not included – this likely explains the less complete coupling of $T_{\rm e}$ to the radiation field at these early epochs). Afterwards γ-ray heating dominates the total heating rate and controls the kinetic temperature. Although the γ-ray heating decreases smoothly with time, $T_{\rm e}$ shows distinct changes. These arise when recombination from one dominant ion to the next occurs and the contributing cooling processes change abruptly. In order to retain the balance

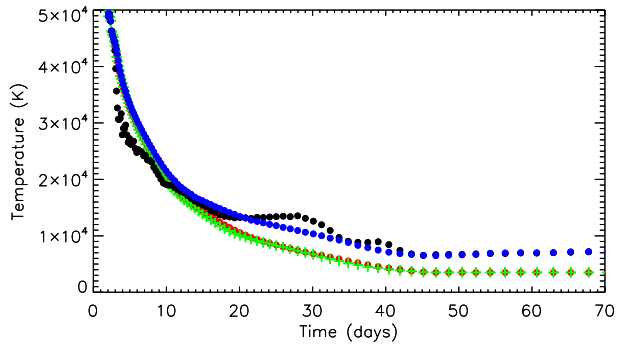

Figure 4. Temperature evolution at a radial velocity of $9590\,\mathrm{km\,s^{-1}}$ i.e. at the outer edge of the iron-rich core. The green crosses show T_J in the simple ionisation treatment. The circles are the three temperatures used in the detailed ionisation treatment and show the kinetic temperature T_e (black), the radiation temperature T_R (blue) and T_J (red). At around 45 days, T_J hits the lower temperature boundary of 3500 K and is not allowed to drop further.

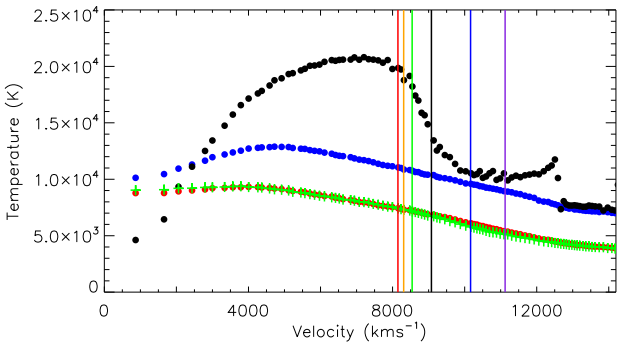

Figure 5. Radial temperature distribution at 31 days after the explosion. The outer layers of the model, which consist only of unburned material and extend up to $22\,800\,\mathrm{km\,s^{-1}}$, are not shown. The green crosses show T_J in the simple ionisation treatment. The circles are the three temperatures used in the detailed ionisation treatment and show the kinetic temperature T_e in black, the radiation temperature T_R in blue and T_J in red. The black/violet/blue/green/red/orange vertical lines show the mean radii of last scattering in bolometric/U/B/V/R/I light. The sharp drop in T_e around $12\,500\,\mathrm{km\,s^{-1}}$ is associated with a strong change in composition in the W7 model. The iron group abundance abruptly drops at this point and intermediate-mass elements dominate.

between the heating and cooling rates then T_e must change rapidly.

Figure 5 illustrates the radial temperature distribution at 31 days after the explosion. T_J for the two different ionisation treatments shows no strong difference. However T_R in the detailed ionisation treatment differs strongly from T_J over the entire ejecta, indicating that the radiation field is bluer and more dilute that would be implied by our radiation field model in the simple ionisation treatment. The kinetic temperature is mainly controlled by γ-ray heating which dominates over the other heating rates outside $\sim 2500\,\mathrm{km\,s^{-1}}$ and varies only gradually with velocity, declining outwards. This leads to $T_\mathrm{e} > T_\mathrm{R}$. Around recombination fronts the contributing cooling processes change abruptly. This means that T_e has to change rapidly in such regions in order that the heating rate remains balanced by the total cooling rate and leads to the rapid decline in T_e between 8000 and 10 000 km/s where the recombination from Fe III to Fe II happens (compare Figure 3). The vertical lines show the mean radii of last scattering for packets which had their last scattering at $\sim$ 31 days. Because of line blocking the optical depths are biggest in the UV and blue and the different bands probe deeper into the ejecta in a sequence from blue to red. An exception is the mean radius of last scattering in the I band which lies at $\sim 8500\,\mathrm{km\,s^{-1}}$, between the R and V bands. This is because the I band has significant contribution from the Ca II NIR triplet which forms outside the iron-rich core.

That the ejecta stay more ionised for longer in the detailed ionisation description has a direct influence on the spectra at late times. This is illustrated in Figure 6 which shows spectra for 15, 20, 40 and 60 days after the explosion for the simple and detailed ionisation treatments. While there are no differences up to about maximum light in B band at 20 days, the spectra calculated using the detailed ionisation treatment are significantly bluer at late times. This is because they still have more Fe II contribution relative to Fe I than the spectra using the simple ionisation treatment (Fe II has bluer lines). The simple ionisation treatment shifts more flux into the red and NIR leading to a strong Fe I emission feature at 60 days which is not seen in observations.

The same effect influences the broad band light curves calculated using the simple and detailed ionisation treatment which are shown in Figure 7. The band passes of Bessell (1990) and Bessell & Brett (1988) are shown in the top panel of Figure 6 to clarify the following discussion. Like the spectra, the light curves are rather similar before maximum light in B band at $\sim$ 20 days, with slight differences in the NIR bands. After maximum light there are strong differences. The U, B and V light curves calculated using the simple ionisation treatment fade much quicker than those using the detailed ionisation treatment. In contrast, R, I, J, H and K stay brighter with J showing a third maximum which is associated with the appearance of the strong Fe I emission feature in the bottom right panel of Figure 6 at about 60 days.

Of particular interest is the R band which shows a clear secondary maximum using the detailed ionisation treatment but only a slight plateau using the simple ionisation treatment. As pointed out by Kasen (2006), the secondary maximum forms when the zone in which doubly ionised iron group elements recombine hits the inner iron-rich core. It is then that the redistribution of flux from the UV and blue part of the spectrum into the red and NIR by fluorescence is most effective. This argumentation is confirmed and explains the differences in the R band light curve between the simple and the detailed ionisation treatment. In the right panels of Figure 3, which shows the ionisation fractions of Fe as a function of time at the outer edge of the iron-rich inner core, we see that for the simple ionisation treatment (top panel) the transition from Fe III to Fe II happens at $\sim$ 33 days while it occurs at $\sim$ 36 days in the detailed ionisation treatment. These times correspond to the times of the secondary maximum of the R band light curve in Figure 7.

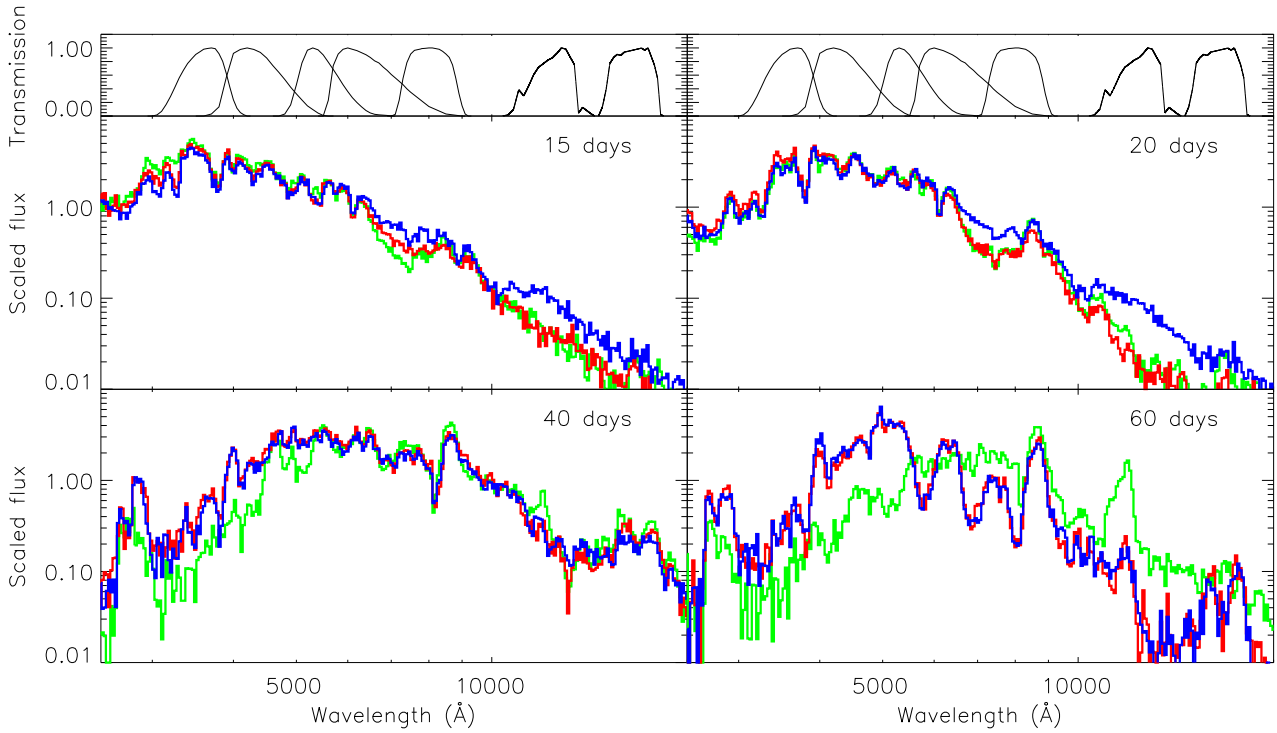

Figure 6. Spectra for the W7 explosion model at 15, 20, 40 and 60 days after the explosion, respectively. The green and red lines were calculated with the cd23_gf-5 atomic dataset using the simple and detailed ionisation treatment, respectively. The blue line was calculated with the big_gf-4 atomic dataset and the detailed ionisation treatment. The top panels show (from left to right) the normalised U,B,V,R,I,J and H passbands of Bessell (1990) and Bessell & Brett (1988).

Thus, with the simple ionisation treatment, the secondary maximum is blended in the first peak such that it is not clearly evident in the light curves.

Taking into account all the effects which have been discussed in this section we conclude that a detailed treatment of ionisation, consistent with the properties of the radiation field, has an important influence and is needed to obtain reliable broad-band light curves and spectra after maximum light. In particular, we note that the colour evolution obtained from calculations using a simple LTE description of ionisation is subject to strong uncertainties.

3.2 Influence of atomic data

As already mentioned, the vast number of line transitions associated with the iron group elements are the main contributors to the opacity. Furthermore the lines provide an efficient way to redistribute radiation from the ultraviolet and blue part of the spectrum into the red and NIR by fluorescence (Pinto & Eastman 2000). This is illustrated in Figure 8 which shows, for 20 days after explosion, the wavelength at which escaping photon packets were emitted versus the wavelength at which the same packets had been last absorbed prior to escape (using atomic dataset cd23_gf-5 and the detailed ionisation treatment). It shows that many absorptions in the UV are followed by emission in the red and NIR, but also that the reverse process happens too (see discussion by Mazzali 2000; Sauer et al. 2008). From the colour coding we see that the iron group elements are most effective in this redistribution.

Figure 9 shows the redistribution at 35 days after the explosion with escaping photon packets binned into a wavelength grid, and indicating how many packets escaped in a bin by its grey shade. Thus individual strong lines become visible. The dark dots at $\lambda_{\rm out} \sim 8600$ Å are associated with emission in the Ca II NIR triplet which results from absorption in the Ca II H and K lines at $\lambda_{\rm in} \sim 4000$ Å as well as from resonance scattering in the NIR triplet itself. In a similar way the Si II line at ~ 6355 Å shows up as a resonance line and in fluorescence with photons absorbed at ~ 4000 Å. This underlines that a fully detailed treatment of line formation is needed to make reliable predictions of individual spectral features and to a lesser extent also for the broad-band light curves. Especially the I band light curve will be affected since it has a strong contribution from the Ca II NIR triplet (see top panels of Figure 6).

To simulate this redistribution properly an atomic dataset as complete as possible is desirable. Unfortunately the simulations become more and more expensive for bigger atomic datasets and the atomic data is not completely known. Thus in the following we study the effect of incomplete atomic data by using datasets of different completeness to calculate the spectral evolution of W7.

We started with the line list of Kurucz & Bell (1995) and tried to reproduce the results of the previous section using atomic datasets with cuts of -2 and -3 in $\log(gf)$ compared to -5 which was used so far (see Table 1 for details on the atomic data). The light curves obtained with the -2 cut

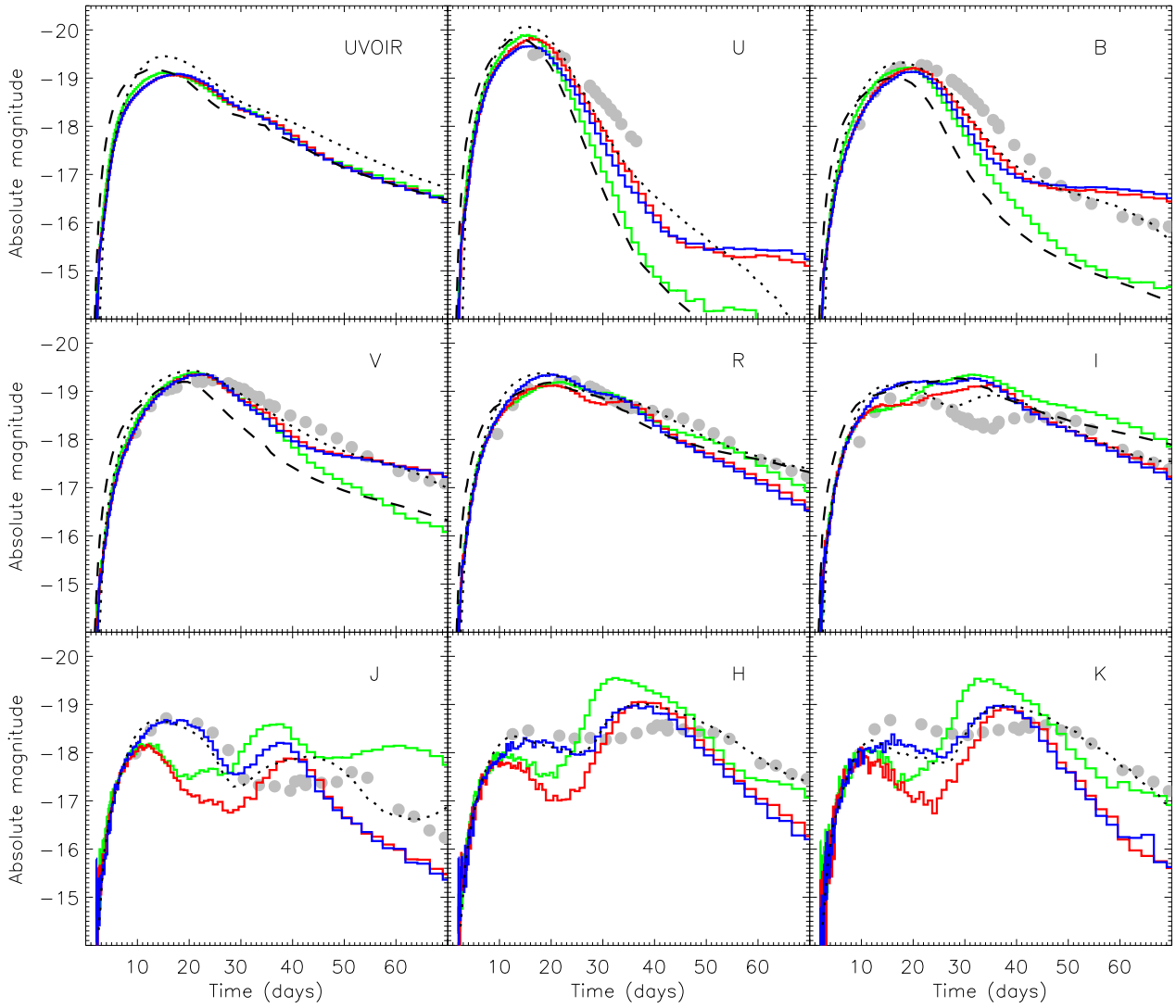

Figure 7. *UVOIR* bolometric and *U,B,V,R,I,J,H,K* light curves for the W7 explosion model. The green/red lines are the light curves obtained with the simple/detailed ionisation treatment and atomic dataset cd23_gf-5. The blue lines are calculated with the detailed ionisation treatment and atomic dataset big_gf-4. The small fluctuations e.g. in the *U* light curve of the simple ionisation treatment and the NIR light curves are due to Monte Carlo noise. For comparison observations of SN 2001el (Krisciunas et al. 2003) are overplotted as grey circles assuming a distance modulus of 31.54 and the reddening law of Cardelli et al. (1989) with $A_V = 0.5$ and $R_V = 3.1$. Furthermore W7 light curves obtained with the Monte Carlo radiative transfer code SEDONA (Kasen priv. comm.; *UVOIR,U,B,V,R,I,J,H,K* dotted lines) and the radiation hydrodynamics code STELLA (Sorokina priv. comm.; *UVOIR,U,B,V,R,I* dashed lines) are shown.

differ strongly from the previous ones, indicating that lines weaker than -2 in $\log(gf)$ play an important role. With the -3 cut, the light curves in the optical bands are almost identical but there are still some minor differences in the NIR bands. Going further to a -20 cut does not change the results compared to the -5 cut. So the cd23_gf-5 atomic dataset, which was used above, is sufficient to simulate the redistribution which is possible within the line list of Kurucz & Bell (1995).

However, this line list with its meagre total of $\sim 5 \cdot 10^5$ lines, contains only a tiny fraction of the millions of lines expected of the iron group elements. As many of these lines are associated with transitions amongst highly excited levels, this line list lacks especially lines in the red and NIR parts of the spectrum. It was pointed out by Kasen et al. (2006) and Kasen (2006) that these missing lines are crucial to obtain light curves in good agreement with observations, especially in the NIR. To study this, we use atomic dataset big_gf-4 (for details see Table 1 and Section 2.3) which includes atomic data for Fe II, Fe III, Co II, Co III, Ni II and Ni III from more modern theoretical computations, increasing the number of lines by a factor of ~ 20 compared to the cd23_gf-5 atomic dataset.

The bolometric and broad-band light curves obtained for the W7 model using the detailed ionisation treatment and atomic dataset big_gf-4 are shown by the blue line in Figure 7. *UVOIR* bolometric and the *U*, *B* and *V* light curves are not strongly affected. In contrast, the enhanced

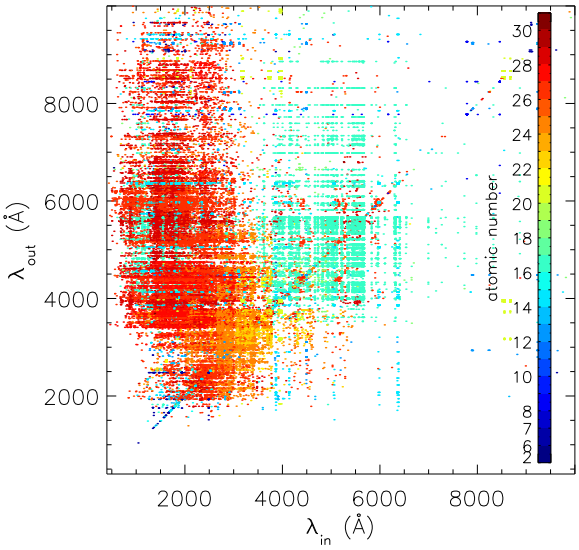

Figure 8. Wavelength redistribution in the last line transition of photon packets which escaped at 20 days after the explosion. Each point displays the wavelength of an escaping photon packet versus the wavelength at which the same packet had been absorbed immediately before emission. Thereby a single point can represent multiple photon packets which have undergone the same absorption and emission processes before they escaped. Points on the diagonal line are photon packets which last undergone resonance scattering. Points above (below) that line have been redistributed into the red (blue) by (reverse) fluorescence. The colour coding shows by which element an escaping photon was last emitted (atomic numbers refer to the colour on top of the number centre) thus indicating that the iron group elements are most efficient in redistributing flux into the red by fluorescence. The data were extracted from our W7 calculation using the detailed ionisation treatment and the cd23_gf-5 model atom.

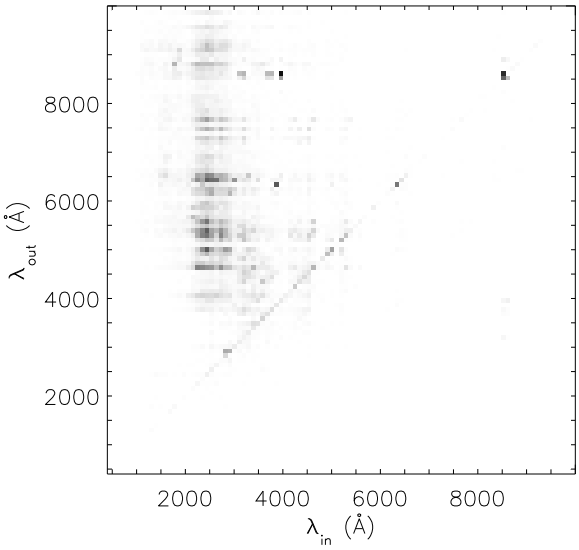

Figure 9. Wavelength redistribution in the last line transition of photon packets which escaped at 35 days after the explosion. The escaping photon packets have been binned into a wavelength grid. The shade of a grid point indicates how many photon packets escaped in this bin (the darker the more packets escaped). Points on the diagonal line are photon packets which last underwent resonance scattering. Points above (below) that line have been redistributed into the red (blue) by (reverse) fluorescence. The dark dots at $\lambda_{\rm out} \sim 8600$ Å and ~ 6300 Å show the flux redistribution from the Ca II H and K lines into the Ca II NIR triplet and in Si II respectively. The data were extracted from our W7 calculation using the detailed ionisation treatment and the cd23_gf-5 model atom.

redistribution of flux from the UV and blue to the red and NIR at early times, which can be seen comparing the red and blue curves in the top panels of Figure 6, increases the first peak in the R, I, J, H and K bands and causes strong differences for $t \lesssim 40$ days. As a consequence of this redistribution, the U and B band light curves using the big_gf-4 atomic dataset are slightly dimmer between ~ 10 and ~ 40 days than those using the cd23_gf-5 atomic dataset. At later times, the light curves are very similar.

The increase in the magnitude of the primary peak in the NIR brings the model light curves to better agreement with observations. The distinct secondary maximum which is present in the R band light curve using the cd23_gf-5 atomic dataset changes – as it is observed – to a shoulder using atomic dataset big_gf-4. However it occurs too early compared to the observations and especially the H and K bands show systematic differences from the observations having secondary peaks brighter than their primary peaks. This could be due to a further lack of atomic data, which might increase the redistribution into the H and K bands. However, calculations with the big_gf-3 atomic dataset (see Table 1), which has fewer lines by a factor of ~ 2, do not show significant differences around the first peaks, suggesting that very weak lines are not critical in this. It is possible, however, that the atomic data set in use is still not complete in terms of lines stronger than a -4 cut in $\log(gf)$ – which we cannot exclude – or that more iron group elements or ions should be included from the comprehensive atomic data set (Kurucz 2006). However memory limitations and computational costs become a severe issue if the atomic data are to be significantly expanded and we note that the small abundances of the other iron group elements suggest that they are less likely to have a major effect. Alternatively, the explosion model itself may be at fault. In particular in a model where the recombination front from doubly to singly ionised material hits the iron-rich inner core later, the secondary maxima would be dimmer and in better agreement with observations. However, investigating more modern explosion models is beyond the scope of this work and will be addressed in future studies.

3.3 Comparison with other codes

We now compare our bolometric and broad-band light curves with those obtained with other radiative transfer codes for the W7 model. We start with the light curves from the multi-energy group radiation hydrodynamics code STELLA (Blinnikov et al. 2006) which treats the line opacity in the expansion opacity formalism (Karp et al. 1977;

Friend & Castor 1983; Eastman & Pinto 1993). E. Sorokina (priv. comm.) provided us with bolometric, U, B, V, R and I light curves calculated with an updated version of this code using a line list of $\sim 1.6 \cdot 10^5$ lines. In this approach, matter is treated in LTE and redistribution is modelled using an approximate source function. The light curves are shown in Figure 7: aside from having earlier peaks, even in bolometric light, these light curves are very similar to our light curves calculated in the simple ionisation treatment with atomic dataset cd23_gf-5. This is not surprising since our simple ionisation description is appropriate for LTE and the atomic data sets are of comparable size. The obvious difference around the first peak in the I band, which is dominated by the Ca II NIR triplet, is most likely due to our more complete treatment of fluorescence. Compared to our detailed ionisation treatment the same remarks as made in Section 3.1 apply.

We also show light curves obtained with the 3D Monte Carlo radiative transfer code SEDONA (Kasen et al. 2006). SEDONA uses the expansion opacity formalism but is capable of treating fluorescence with a more sophisticated approximation for a subset of lines using a downward-branching scheme. When a photon is absorbed by a line treated in the expansion opacity formalism a two-level atom (TLA) approximation is used and the photon undergoes coherent scattering with probability $1 - \epsilon$. Otherwise it is absorbed and reemitted at a wavelength sampled from the local thermal emissivity, thus representing both true absorption and fluorescence. In principle ϵ is a unique parameter for each line, however SEDONA usually uses a common value for all lines [see Kasen et al. (2006) for a discussion]. Matter is treated in LTE with the local kinetic temperature being derived from balancing the thermal emissivity with the energy deposition by γ-ray heating and photon absorption recorded during the Monte Carlo simulations. The light curves shown in Figure 7 were provided by D. Kasen (priv. comm.) and use a line list of $\sim 10^7$ lines treated in the TLA approximation.

The light curves are in good agreement with our calculations using the big_gf-4 atomic dataset up to maximum light. After maximum light some differences manifest. The SEDONA U and B light curves after 50 days decline faster than ours – this may be because of recombination to the neutral state, which is responsible for the relatively rapid decay of the U and B light curves obtained with our simple ionisation treatment (see Section 3.1). Note that, despite using LTE conditions to describe the matter state, the SEDONA light curves do not fade as quickly after maximum light as those obtained with STELLA or with our simple ionisation treatment (which is equivalent to treating matter in LTE). This is likely to be due to the different manner in which the kinetic temperature is computed by the different codes.

The V band light curves are almost identical. In the NIR light curves we get remarkably similar results up to $\sim$ 40 days. Afterwards, the SEDONA light curves stay brighter. Since we have seen in Section 3.1 that a more complete recombination leads to an increased redistribution of flux into the red and NIR by Fe I and Co I this is presumably due to a more complete recombination compared to our calculation. The strong differences in the I band light curve are most likely due to the different treatment of line formation. The flux in the I band is dominated by the Ca II NIR triplet for which the SEDONA light curves shown here assume pure scattering ($\epsilon = 0$, see the discussion in Kasen 2006), while we treat the line formation in full detail.

4 APPLICATION TO AN ELLIPSOIDAL TOY MODEL

In this section we use an ellipsoidal toy model to demonstrate the multi-dimensional capabilities of the code and to illustrate the basic effects which large-scale ejecta asymmetries introduce in spectra and light curves. Large-scale asymmetries in the ejecta of SNe Ia are suggested both by observed polarimetry [see Wang & Wheeler (2008) for a review] as well as by theoretical explosion models [e.g. from an off-centre ignition condition (Röpke, Woosley & Hillebrandt 2007), a deflagration to detonation transition (Röpke & Niemeyer 2007) or in the gravitationally confined explosion scenario (Plewa, Calder & Lamb 2004)]. We stress that the toy model we employ here is extremely simple and has a much stronger asphericity than the observations or theoretical arguments suggest. However, it is a useful test case for our code which clearly identifies the sense of the effects acting on the spectra and light curves.

4.1 The model

Taking the total mass and composition of the W7 model and assuming homologous expansion, we constructed a simple ellipsoidal toy model assuming rotational symmetry about the z-axis. The maximum velocities along the x- and y-axes are set to be only half the maximum velocity ($v_z^{\max} = 27\,500\,\mathrm{km\,s^{-1}}$) along the z-axis, thus giving an axis-ratio of 1:1:2. Within the model, ellipsoidal surfaces are taken as surfaces of constant density and we adopt a density profile

$$\rho(v) \propto \exp\left(\sqrt{v_\mathrm{r}^2 + \left(\frac{v_\mathrm{z}}{2}\right)^2}/v_0\right) \tag{19}$$

in cylindrical polar coordinates and $v_0 = 2750\,\mathrm{km\,s^{-1}}$. We assume a stratified composition with three zones. The innermost zone contains all the iron group material (Sc to Zn) and is surrounded by a zone of intermediate mass elements (F to Ca). The outermost zone contains the unburned material (He,C,N,O). Inside each zone the relative abundances are homogeneous and kept fixed at their W7 values.

We mapped this model to a 64^3 grid and followed the propagation of $3.2 \cdot 10^7$ energy packets over 100 time steps from 2 to 80 days after the explosion, using the cd23_gf-5 atomic dataset and the detailed ionisation treatment. The first 10 time steps have been calculated in the simple ionisation treatment to get reliable initial values (see the discussion in Section 2.2.2). To save computational time we make use of our initial grey approximation setting $\tau_{\mathrm{Th,min}} = 15$ and $N_{\mathrm{grey}} = 40$ (see Section 2.1.6). Spectra and light curves were obtained by binning the escaping packets in 10 equal solid angle bins centred around the z-axis.

4.2 Spectral evolution

In Figure 10 we compare the 2500 to 10 000 Å spectra along the major and minor axes with an angle averaged spectrum

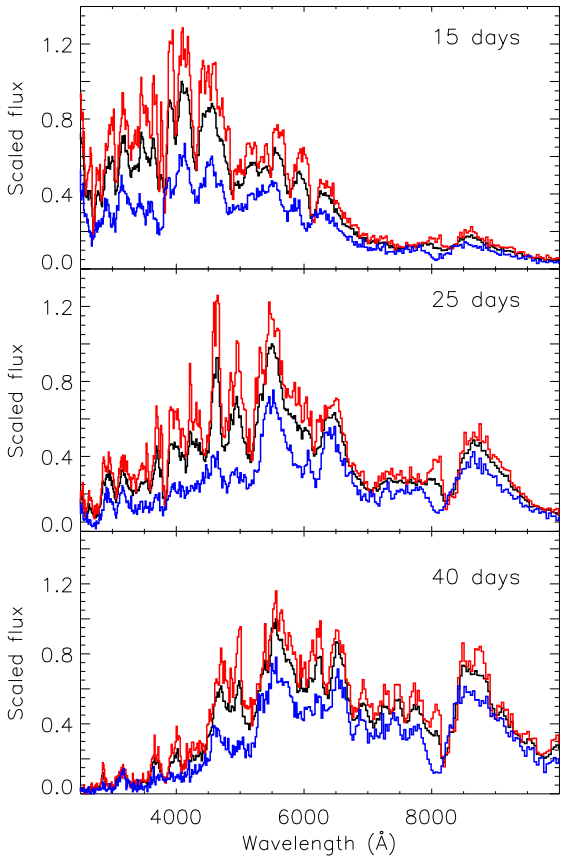

Figure 10. Spectra for the ellipsoidal toy model at 15, 25 and 40 days after the explosion (from top to bottom). Blue/red lines are for viewing down the major/minor axis. The black line shows an angle-averaged spectrum for comparison.

for 15 (around maximum light in B band), 25 and 40 days after explosion. In the absorption trough of the P Cyg feature of the Ca II NIR triplet one clearly sees the different velocity extent along the different axes: viewed down the major axis, the escaping photons see a velocity field twice as large compared to the minor axes such that the absorption troughs extend farther into the blue. In general the spectra along the minor axes show much sharper features than those along the major axis, where the higher velocities cause stronger blending.

Furthermore the total flux observed along the minor axis is larger. This can be understood by a simple geometrical argument. Viewed down the minor axis the cross-section surface of our ellipsoid is twice as big as seen down the major axis. For an opaque ellipsoid of uniform surface brightness, we would expect the same ratio for the flux (i.e. $\Delta M_{\rm geom} \approx -0.75$ in magnitudes). However, additional effects come into play such that the flux difference between major and minor axis depends on wavelength and time as discussed below.

4.3 Broad-band light curves

The broad-band light curves are shown in Figure 11. As expected, the light curves observed along the minor axes are always brighter than those observed along the major axis. The viewing-angle effect is always strongest in the bluer bands and after maximum light becomes weaker with time in V and redder bands (see Table 2) as the ejecta become optically thin in these parts of the spectrum.

Table 2. $\Delta M = M_{\rm minor} - M_{\rm major}$ for selected bands in the ellipsoidal model at different times after explosion.

t	15d	22d	29d	35d	42d	49d
$\Delta M(U)$	-0.93	-1.01	-0.92	-0.80	-0.70	-0.87
$\Delta M(V)$	-0.52	-0.65	-0.54	-0.48	-0.45	-0.46
$\Delta M(I)$	-0.42	-0.41	-0.35	-0.36	-0.34	-0.23
$\Delta M(H)$	-0.38	-0.24	-0.22	-0.27	-0.27	-0.19

Table 3. Peak times and ΔM_{15} for selected bands in the ellipsoidal model.

	$t_{\rm max}^{\rm major}$ (d)	$t_{\rm max}^{\rm minor}$ (d)	$\Delta M_{15}^{\rm major}$	$\Delta M_{15}^{\rm minor}$
UVOIR	14.7	15.8	-0.6	-0.9
U	11.8	13.7	-1.7	-1.9
B	15.2	15.8	-1.7	-1.8
V	18.3	19.0	-0.9	-1.1
R	19.0	19.0	-0.5	-0.6

In the U and B bands, which stay optically thick throughout our calculation, this effect remains significant until the latest times of our simulation and the difference $\Delta M = M_{\rm minor} - M_{\rm major}$ is even bigger than one would expect from the simple geometrical argument (which would imply $\Delta M_{\rm geom} \approx -0.75$; see above). This is simply because we do not have an opaque ellipsoid of uniform surface brightness. In fact, Figure 12 – which illustrates the region of last emission (RLE) of selected bands at different times – shows that the U band RLE is concentrated around the equatorial plane which acts to amplify the geometrical effect (as long as the ejecta are optically thick, the direction of escape tends to be peaked normal to the contours of constant density). This concentration is a consequence of the large number of highly optically thick Fe group lines in the UV: U band photons are more strongly trapped than photons in other bands and therefore tend to preferentially leak out along the equatorial plane where the velocity swept out is smallest.

In contrast, the RLE of V and redder bands do not show a strong enhancement around the equatorial plane. The V band RLE around maximum light is nearly ellipsoidal, making ΔM close to $\Delta M_{\rm geom}$. At later times, the emission becomes more isotropic as the ejecta become optically thinner (in Figure 12 the whole ellipsoid contributes to the RLE) and ΔM decreases. For the I and H band, in which ΔM is always less than $\Delta M_{\rm geom}$, the ejecta are already becoming optically thin around maximum light.

The H band RLE shows a slight enhancement towards the polar regions around maximum light. This is related to the reduced U band emission in these regions. The high optical depths for blue and UV photons mean that fluorescence redistributes flux into the NIR where optical depths are lower such that the radiation can escape.

In general the NIR light curves are least viewing-angle dependent, thus supporting the use of NIR light curves for cosmological distance measurements since less intrinsic scat-

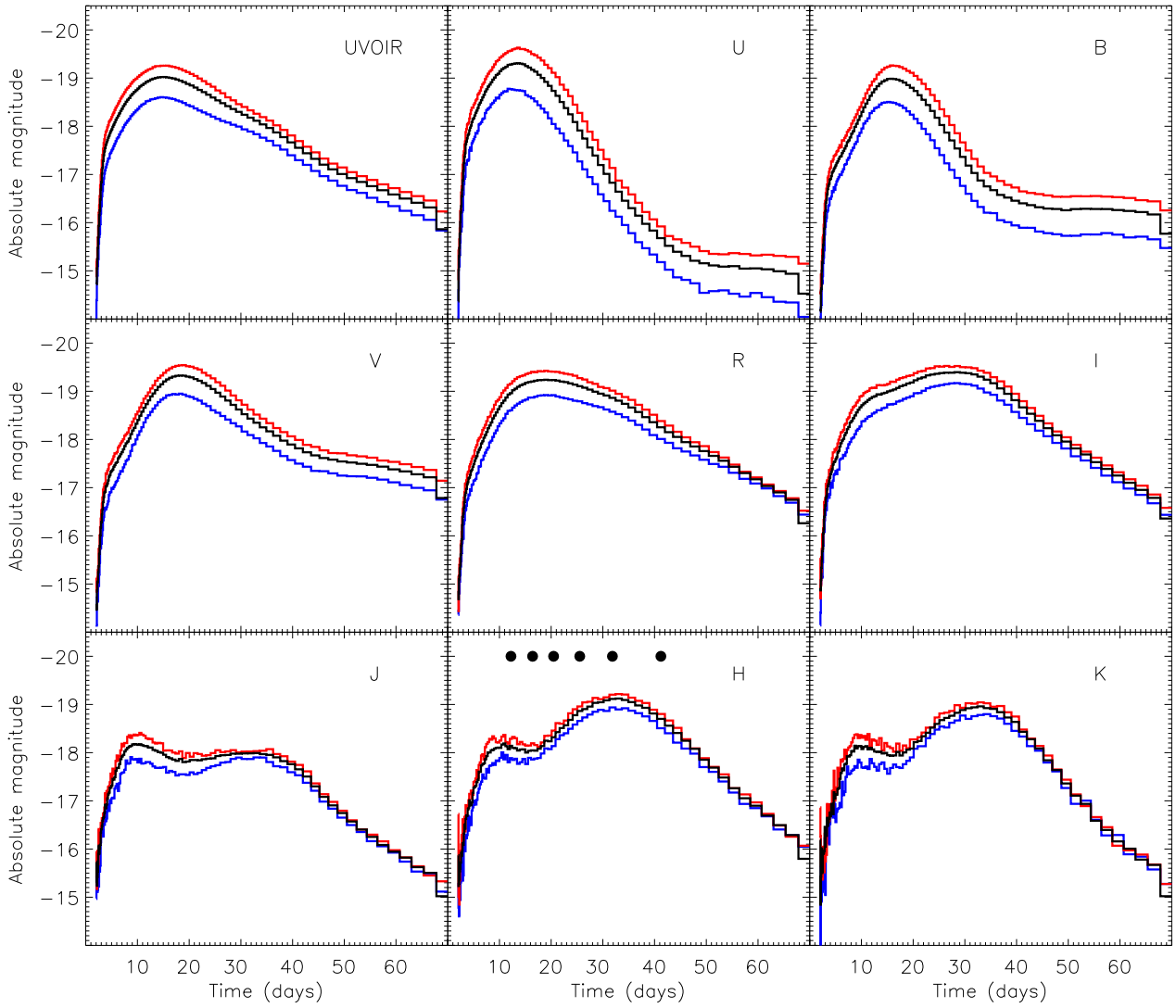

Figure 11. *UVOIR* bolometric and *U,B,V,R,I,J,H,K* light curves for the ellipsoidal toy model. The blue/red lines are the light curves obtained along the major/minor axis. The black line shows an angle-averaged light curve for comparison. The filled circles in the *H*-band panel indicate the times for which snapshots of the ionisation state of Fe are shown in Figure 13.

ter would be expected if geometry effects have any role in the observed properties of SNe Ia. However more detailed studies are needed to investigate this.

The light curves observed along the major axis peak slightly earlier than those observed along the minor axes (see Table 3). Furthermore light curves observed along the major axis decline more slowly than those observed along the minor axes (compare the ΔM_{15}[3] values in Table 3). A similar effect was already found in a study using a grey version of our code by Sim (2007), and we note that it is opposite to the sense of the observed light curve width-luminosity relation.

The plot showing the regions of last emission in Figure 12 also traces the stratified composition of our model. The *U* and *I* bands – which have non-negligible contributions of Ca due to the Ca II H and K lines in *U* and the Ca II NIR triplet in *I* – show significant emission from the zone of intermediate mass elements. In contrast, the RLE in the *V* and *H* bands – which are dominated by Fe group elements – is concentrated towards the iron-rich inner core.

4.4 Secondary maximum in the NIR bands

As discussed by Kasen (2006), the secondary maximum in the NIR bands forms when the inner iron-rich core recombines from doubly ionised iron group elements to the singly ionised state. With the singly ionised state becoming dominant, the number of optically thick lines in the blue increases, thus blocking blue radiation very effectively and making the redistribution of flux from the UV and blue part of the spectrum into the red and NIR by fluorescence very effective. Here we discuss this effect for the *H* band light

[3] ΔM_{15} gives the change in magnitude between maximum light and 15 days after maximum light.

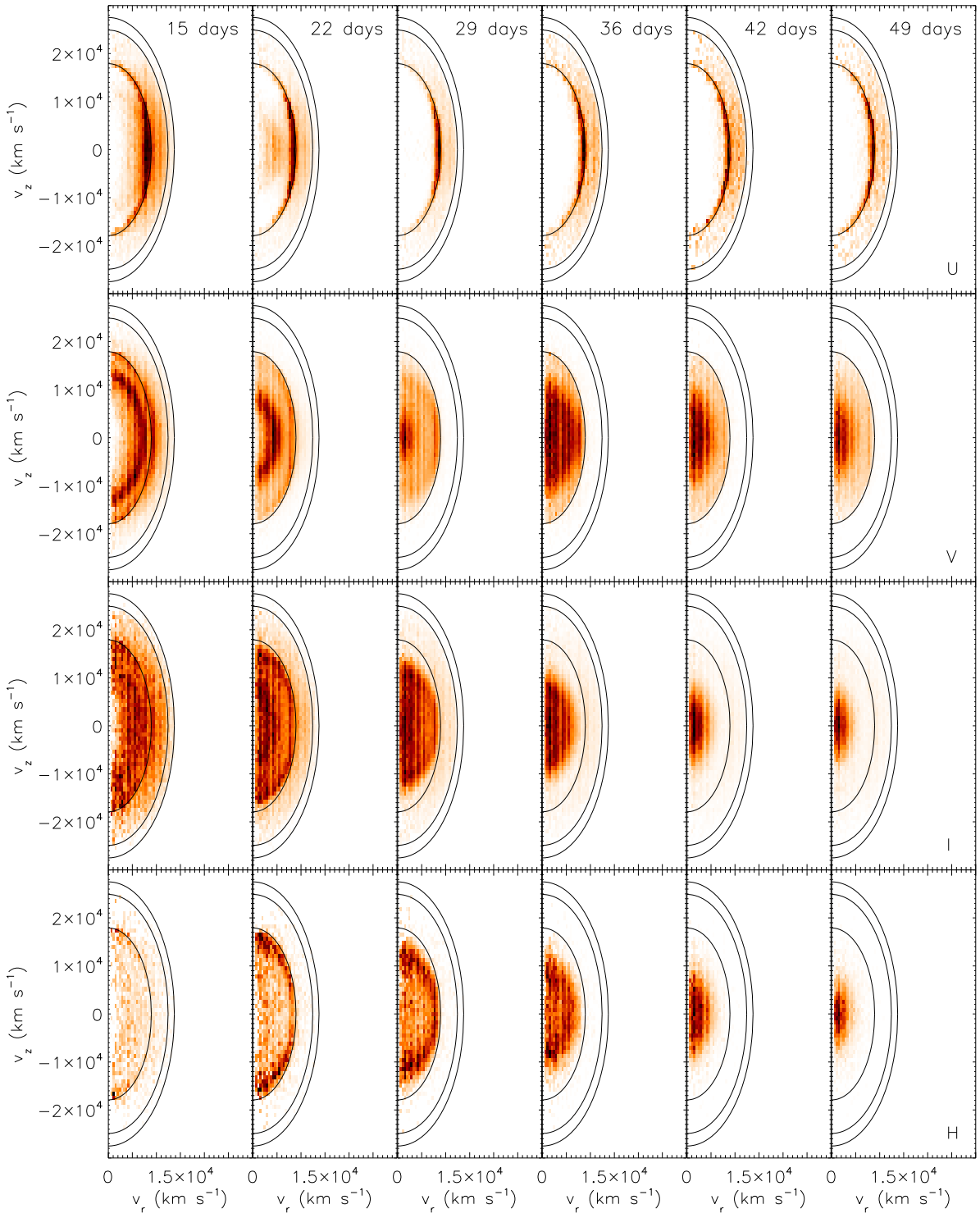

Figure 12. Region of last emission for selected bands (U, V, I, H from top to bottom) and different times (from left to right). Dark regions contribute most to the flux escaping in the band. The solid lines indicate the three zones of different composition, with Sc–Zn in the centre surrounded by F–Ca and finally He,C,N and O in the outer zone. The model is symmetric under rotation about the z-axis.

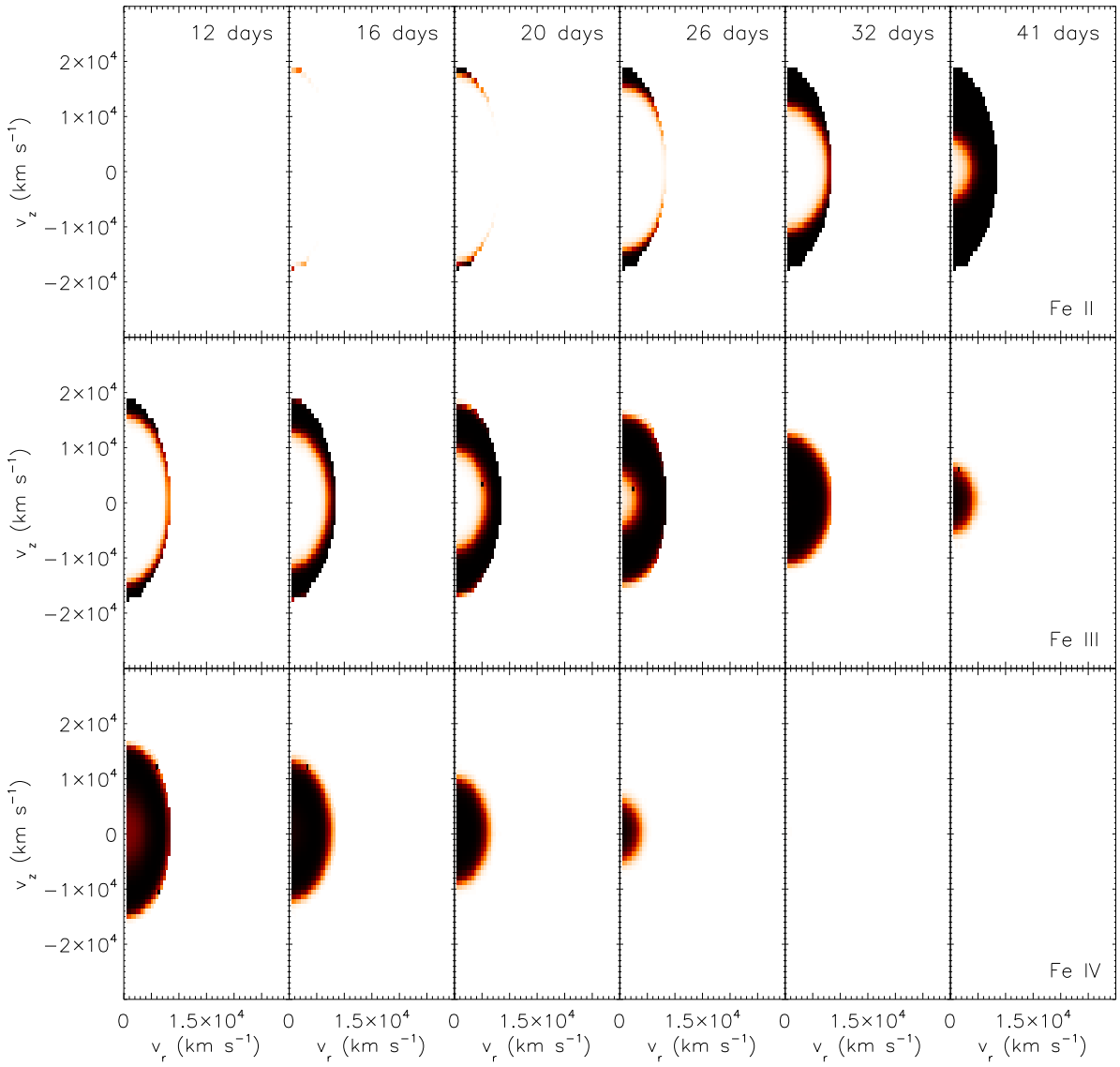

Figure 13. Ionisation fractions of Fe II, Fe III and Fe IV (from top to bottom) for selected times (from left to right). The corresponding times are marked with filled circles in the *H* band panel of Figure 11. Black regions have an ionisation fraction of 1. Lower ionisation fractions are shown in lighter reddish colours down to white (0) on a linear scale.

curve and show the ionisation fractions of Fe II–IV (which we use as a proxy for all iron group elements) in Figure 13 for selected times from near the first peak ($\sim$ 10 days after explosion) to well after the second peak in the *H* band ($\sim$ 32 days after explosion, compare Figure 11).

Around the first peak the iron-rich core consists predominantly of Fe IV. In the very centre there is still a contribution of Fe V (not shown in Figure 13) and at the outer edge there is a small region which has already recombined to Fe III. As time passes the ejecta cool and the Fe IV region recedes. At the same time the Fe III region extends further in and a contribution of Fe II starts to build up around the outsides. Recombination occurs first at the poles since they see the least amount of ionising radiation (compare Figure 12). The secondary maximum in the *H* band occurs at $\sim$ 32 days when the Fe II region first forms a complete elliptical ring (Figure 13). This is the point at which the opportunity for fluorescence is maximal. Note that although the ionisation fractions vary with position, the NIR bands are sufficiently optically thin that the NIR flux is approximately angle-independent at these epochs (this is apparent from Figure 12 where the full ellipsoid is bright). At late times the recombination front moves inwards as the light curves fade until only a small Fe III core remains at the end of our simulation.

Comparing the two different lines-of-sight in Figure 11, we see that the local minimum between the first and secondary maximum in the *H* band light curve along the polar axis occurs slightly earlier ($\sim$ 15 days) than along the equatorial axes ($\sim$ 18 days). This follows from the earlier recombination from Fe III to Fe II in polar lobes which gives

an earlier increase in the redistribution of flux from the UV and blue into the red and NIR.

5 CONCLUSIONS

Based on the approach of Lucy (2002, 2003) we extended the grey time-dependent 3D Monte Carlo radiative transfer code of Sim (2007) to a non-grey opacity treatment. The new code, ARTIS, treats the γ-deposition and spectrum formation in detail and solves the ionisation balance together with the thermal balance equation consistently with the radiation field. Line formation is treated in the Sobolev approximation using the macro-atom approach of Lucy (2002, 2003) to model atomic physics in detail. This allows parameter-free radiative transfer simulations for 3D hydro models with a maximum of predictive power to be made.

We applied this code to the well-studied one-dimensional deflagration model W7 (Nomoto et al. 1984) as a test case and found good agreement with both earlier work using different codes [SEDONA (Kasen et al. 2006); STELLA (Blinnikov & Sorokina 2002; Blinnikov et al. 2006)] and observations [SN 1994D (Patat et al. 1996); SN 2001el (Krisciunas et al. 2003)]. Concerning the NIR light curves, we confirm the importance of line fluorescence in modelling these bands and, particularly their strong dependence on the size of the atomic data set in use. Rather than adopting LTE, we assume photoionisation equilibrium and solve the ionisation balance equations using rates consistent with the radiation field. We showed that this leads to significant differences in the ionisation structure after maximum light, which strongly affect spectra and light curves. The macro-atom formalism allows us to avoid introducing a parameterised treatment of line fluorescence, such that we account for the differing contributions of resonance scattering and fluorescence in different lines (see Figure 9).

To demonstrate the multi-dimensional capabilities of the code we have presented calculations for an ellipsoidal toy model as an example. As expected [e.g. from the grey study by Sim (2007) for a similar model], light curves observed along the minor axes are brighter than those observed along the major axis. The sensitivity decreases with time, as the ejecta become less optically thick, and from blue to red wavelengths. If line-of-sight effects due to asymmetric explosions have a significant influence on the scatter around the Phillips relation of SNe Ia (Phillips 1993), this could explain why the NIR light curves seem to be more homogeneous and thus most promising for cosmological distance measurements. However more detailed studies are needed to investigate this fully for realistic models.

In future work we will extend our method to include a treatment of non-thermal excitation and ionisation which we currently do not treat in detail but which can be important (for a discussion see Baron et al. 1996). This will also allow us to extend the simulations to later epochs (nebular phase) which are strongly affected by these processes. Eventually time-dependent terms in the statistical equilibrium equations could be taken into account and polarisation could be treated, thereby extending the range of data with which we can make meaningful comparisons.

ACKNOWLEDGMENTS

We are very grateful to W. Hillebrandt for stimulating discussions and making this work possible. Furthermore we thank E. Sorokina, S. Blinnikov and D. Kasen for providing us with results of light curve calculations from STELLA and SEDONA and also for useful comments. We also acknowledge helpful discussions with S. Hachinger, F. Röpke, D. Sauer and S. Taubenberger. We thank the anonymous referee for several helpful suggestions.
This work made use of the SUSPECT database.

REFERENCES

Abbott D. C., Lucy L. B., 1985, ApJ, 288, 679
Ambwani K., Sutherland P., 1988, ApJ, 325, 820
Astier P., et al., 2006, A&A, 447, 31
Baron E., Bongard S., Branch D., Hauschildt P. H., 2006, ApJ, 645, 480
Baron E., Hauschildt P. H., Nugent P., Branch D., 1996, MNRAS, 283, 297
Bessell M. S., 1990, PASP, 102, 1181
Bessell M. S., Brett J. M., 1988, PASP, 100, 1134
Blinnikov S., Sorokina E., 2002, eprint arXiv:astro-ph/0212567
Blinnikov S. I., Röpke F. K., Sorokina E. I., Gieseler M., Reinecke M., Travaglio C., Hillebrandt W., Stritzinger M., 2006, A&A, 453, 229
Branch D., Buta R., Falk S. W., McCall M. L., Uomoto A., Wheeler J. C., Wills B. J., Sutherland P. G., 1982, ApJ, 252, L61
Branch D., Lacy C. H., McCall M. L., Sutherland P. G., Uomoto A., Wheeler J. C., Wills B. J., 1983, ApJ, 270, 123
Cardelli J. A., Clayton G. C., Mathis J. S., 1989, ApJ, 345, 245
Colgate S. A., McKee C., 1969, ApJ, 157, 623
Eastman R. G., Pinto P. A., 1993, ApJ, 412, 731
Friend D. B., Castor J. I., 1983, ApJ, 272, 259
Gamezo V. N., Khokhlov A. M., Oran E. S., Chtchelkanova A. Y., Rosenberg R. O., 2003, Sci, 299, 77
Hillebrandt W., Niemeyer J. C., 2000, ARA&A, 38, 191
Höflich P., 1995, ApJ, 443
Höflich P., Stein J., 2002, ApJ, 568, 779
Hoyle F., Fowler W. A., 1960, ApJ, 132, 565
Jeffery D. J., Leibundgut B., Kirshner R. P., Benetti S., Branch D., Sonneborn G., 1992, ApJ, 397, 304
Karp A. H., Lasher G., Chan K. L., Salpeter E. E., 1977, ApJ, 214, 161
Kasen D., 2006, ApJ, 649, 939
Kasen D., Thomas R. C., Nugent P., 2006, ApJ, 651, 366
Krisciunas K., Suntzeff N., Candia P., Arenas J., Espinoza J., Gonzalez D., Gonzalez S., Höflich P., Landolt A., Phillips M., Pizarro S., 2003, AJ, 125, 166
Kuhlen M., Woosley S. E., Glatzmaier G. A., 2006, ApJ, 640, 407
Kurucz R., Bell B., 1995, Atomic Line Data, Kurucz CD-ROM No. 23., Cambridge, Mass.: Smithsonian Astrophysical Observatory.
Kurucz R. L., 2006, in Stee P., ed., Radiative Transfer and Applications to Very Large Telescopes Vol. 18 of EAS Publications Series, Including all the Lines. pp 129–155

Lamers H. J. G. L. M., Cassinelli J. P., 1999, Introduction to Stellar Winds. Cambridge University Press
Lentz E. J., Baron E., Branch D., Hauschildt P. H., 2001, ApJ, 557, 266
Livio M., 2000, in Niemeyer J. C., Truran J. W., eds, Type Ia Supernovae, Theory and Cosmology The Progenitors of Type Ia Supernovae. Cambridge University Press, p. 30
Lucy L. B., 1999a, A&A, 344, 282
Lucy L. B., 1999b, A&A, 345, 211
Lucy L. B., 2002, A&A, 384, 725
Lucy L. B., 2003, A&A, 403, 261
Lucy L. B., 2005, A&A, 429, 19
Lucy L. B., Abbott D. C., 1993, ApJ, 405, 738
Maeda K., Mazzali P. A., Nomoto K., 2006, ApJ, 645, 1331
Mazzali P. A., 2000, A&A, 363, 705
Mazzali P. A., Lucy L. B., 1993, A&A, 279, 447
Mihalas D., 1978, Stellar Atmospheres, 2nd edn. W. H. Freeman and Company
Nomoto K., Thielemann F.-K., Yokoi K., 1984, ApJ, 286, 644
Nugent P., Baron E., Branch D., Fisher A., Hauschildt P. H., 1997, ApJ, 485, 812
Patat F., Benetti S., Cappellaro E., Danziger I. J., della Valle M., Mazzali P. A., Turatto M., 1996, MNRAS, 278, 111
Perlmutter S., et al., 1999, ApJ, 517, 565
Phillips M. M., 1993, ApJ, 413, L105
Pinto P. A., Eastman R. G., 2000, ApJ, 530, 757
Plewa T., Calder A. C., Lamb D. Q., 2004, ApJ, 612, L37
Reinecke M., Hillebrandt W., Niemeyer J. C., 2002, A&A, 391, 1167
Riess A. G., et al., 1998, AJ, 116, 1009
Riess A. G., et al., 2004, ApJ, 607, 665
Röpke F. K., 2005, A&A, 432, 969
Röpke F. K., Hillebrandt W., 2005, A&A, 431, 635
Röpke F. K., Niemeyer J. C., 2007, A&A, 464, 683
Röpke F. K., Woosley S. E., Hillebrandt W., 2007, ApJ, 660, 1344
Salvo M. E., Cappellaro E., Mazzali P. A., Benetti S., Danziger I. J., Patat F., Turatto M., 2001, MNRAS, 321, 254
Sauer D. N., Mazzali P. A., Blondin S., Stehle M., Benetti S., Challis P., Filippenko A. V., Kirshner R. P., Li W., Matheson T., 2008, MNRAS, 391, 1605
Shull J. M., van Steenberg M., 1982, ApJS, 48, 95
Sim S. A., 2007, MNRAS, 375, 154
Sim S. A., Mazzali P. A., 2008, MNRAS, 385, 1681
Thielemann F.-K., Nomoto K., Yokoi K., 1986, A&A, 158, 17
Truran J., Arnett D., Cameron A., 1967, Canad. J. Physics, 45, 2315
Verner D. A., Ferland G. J., Korista K. T., Yakovlev D. G., 1996, ApJ, 465, 487
Verner D. A., Yakovlev D. G., 1995, A&AS, 109, 125
Wang L., Wheeler J. C., 2008, ARA&A, 46, 433
Wood-Vasey W. M., et al., 2007, ApJ, 666, 694

This paper has been typeset from a TEX/ LATEX file prepared by the author.